

maintaining high resolution of 512×512 scanned points. Modification of the ECLIPSE FN1 was necessary for intravital imaging because this upright microscope is originally designed for imaging thin, sectioned slices, and not for live animals. The trans-illumination unit (halogen lamp, condenser, sub-stage and turret) was removed entirely from the microscope, as confocal imaging never requires transmitted light, which allowed for more space between the microscope stage and the objective lens. The motorized stage was set as low as possible onto a customized framework, and a custom-designed height-adjustable mouse stage was fixed onto the motorized stage. Small temperature controller (Thermoplate; Tokai Hit Co., Ltd., Shizuoka, Japan) was integrated to the mouse stage [Fig. 1(a)]. For sample imaging, a custom-designed height adjustable coverslip holder is placed onto the tissue of interest to provide a flat surface for the objective lens [Fig. 1(b)]. The coverslip must be perpendicular to the objective lens, tightly fixed, and rigid enough so that the tissue of interest will not move during the imaging, but not so tight as to restrict blood flow. The detailed blueprint of the custom-designed mouse stage and the coverslip holder (fabricated and assembled by Sigma Koki Co. Ltd., Tokyo, Japan) will be provided upon request.

Fluorescent reagents

Hoechst 33342 dye (8 mg/kg in PBS, Lonza Group Ltd., Basel, Switzerland) was used to stain the nuclei of cells present in circulation and in the perivascular space. Evans Blue dye (8 mg/kg in PBS, Wako Pure Chemical Industries, Ltd., Osaka, Japan), which binds to plasma albumin, was used to stain the vasculature. Fluorescein (4 mg/kg in PBS, molecular weight of 332.31, Alcom Japan, Ltd., Tokyo, Japan) and fluorescein-labeled dextrans with average molecular weights of 10k, 70k, 500k (Invitrogen Corporation, Carlsbad, CA, USA) were used to study molecular weight-dependent pharmacokinetics. For the comparison study of normal and hydrodynamic injection, psFLT-1 plasmid DNA was labeled with Cy5 using Label IT Tracker Nucleic Acid Localization Kits (Mirus Bio Corporation, Madison, WI, USA).

Surgical procedures

All animal experimental procedures were executed in accordance with the Guide for the Care and Use of Laboratory Animals as stated by the National Institutes of Health. Mice were anesthetized with 2.0-3.0% isoflurane (Abbott Japan Co., Ltd., Tokyo, Japan) using a Univentor 400 Anaesthesia Unit (Univentor Ltd., Zejtun, Malta). Mice were then subjected to lateral tail vein catheterization with a 30-gauge needle (Becton, Dickinson and Co, Franklin Lakes, NJ, USA) connected to a non-toxic, medical grade polyethylene tube (Natsume Seisakusho Co., Ltd., Tokyo, Japan). Catheterization technique is described elsewhere (<http://imaging.bme.ucdavis.edu/surgical.html>). This catheterization allows multiple and timed injection without moving the mouse during data acquisition.

Ear lobe dermis tissue was accessible without surgery and easily fixed beneath the cover slip with a single drop of immersion oil. Tumor, kidney, or liver tissues were accessed following exteriorization through skin incision. For tumor imaging, female BALB/c nude mice were inoculated subcutaneously with H2B-GFP cells, which express green fluorescence protein in cell nuclei. Tumors were allowed to mature until the size of the tumor reached 5 mm in diameter. To minimize bleeding during the surgical procedure required to present tumors for imaging, a Surgitron (R) radio-frequency surgical device equipped with a Vari-Tip (TM) Wire Electrode (Cat. No. A8D) (Ellman International Inc., Oceanside, NY, USA) was used for bloodless, micro smooth incision with minimal tissue alteration.

Movie and time-lapse image acquisition

Video acquisition at a speed of 30 frames per second was performed for the indicated times, followed by time-lapse imaging every 1 minute. Drugs were administered via the tail vein catheter 10 seconds after video acquisition was initiated.

Acknowledgments

We thank Teru Kanda (Aichi Cancer Center Research Institute) for HeLa H2B-GFP cells. We thank Masabumi Shibuya (Tokyo Medical and Dental University) for providing pVL 1393 baculovirus vector pDNA encoding human sFLT-1. We thank Yoko Hasegawa, Mika Zenibayashi, Kotoe Date, Satomi Ogura, and Katsue Morii (The University of Tokyo) for technical assistance. T.O. is an employee of Nikon Instech Co., Ltd. All other authors declare no conflict of interest. This work was supported by Core Research Program for Evolutional Science and Technology (CREST) from the Japan Science and Technology Corporation (JST) (K.K.), Funding Program for World-Leading Innovative R&D on Science and Technology (FIRST Program) from Japan Society for the Promotion of Science (JSPS)(K.K.), and Grants-in-Aid for Scientific Research from the Japanese Ministry of Education, Culture, Sports, Science and Technology of Japan (21890051) (Y.M.).

DRUG DELIVERY

Improving Drug Potency and Efficacy by Nanocarrier-Mediated Subcellular Targeting

Mami Murakami,¹ Horacio Cabral,^{1,2} Yu Matsumoto,³ Shourong Wu,³ Mitsunobu R. Kano,⁴ Takao Yamori,⁵ Nobuhiro Nishiyama,^{2,3*} Kazunori Kataoka^{1,2,3,6*}

Nanocarrier-mediated drug targeting is an emerging strategy for cancer therapy and is being used, for example, with chemotherapeutic agents for ovarian cancer. Nanocarriers are selectively accumulated in tumors as a result of their enhanced permeability and retention of macromolecules, thereby enhancing the antitumor activity of the nanocarrier-associated drugs. We investigated the real-time subcellular fate of polymeric micelles incorporating (1,2-diaminocyclohexane) platinum(II) (DACHPt/m), the parent complex of oxaliplatin, in tumor tissues by fluorescence-based assessment of their kinetic stability. These observations revealed that DACHPt/m was extravasated from blood vessels to the tumor tissue and dissociated inside each cell. Furthermore, DACHPt/m selectively dissociated within late endosomes, enhancing drug delivery to the nearby nucleus relative to free oxaliplatin, likely by circumvention of the cytoplasmic detoxification systems such as metallothionein and methionine synthase. Thus, these drug-loaded micelles exhibited higher antitumor activity than did oxaliplatin alone, even against oxaliplatin-resistant tumors. These findings suggest that nanocarriers targeting subcellular compartments may have considerable benefits in clinical applications.

INTRODUCTION

In 2009, about 10 million people worldwide were newly diagnosed with cancer (1). Application of nanotechnology to cancer therapy may offer therapeutic effects that cannot be achieved with other strategies. The main aim of this approach is to develop nanoscale drug vehicles for targeted cancer therapy (2–5). Nanocarriers selectively accumulate in solid tumors as a result of the enhanced permeability and retention (EPR) effect, which is characterized by microvascular hyperpermeability to circulating macromolecules and impaired lymphatic drainage in tumor tissues (6). At present, several nanocarrier formulations have been approved for clinical use against ovarian cancer and HIV-associated Kaposi's sarcoma (Doxil) and breast cancer (Abraxane). These formulations allow better accumulation of the drugs doxorubicin and paclitaxel in tumors (7).

Polymeric micelles, self-assemblies of block copolymers, have gained increasing popularity as tumor-targetable nanocarriers since they were first used as drug vehicles in the late 1980s (8–12). These micelles, which are several tens of nanometers in size and have a characteristic core-shell structure consisting of a drug-loaded hydrophobic core and poly(ethylene glycol) (PEG) hydrophilic shell, are long-lived in the bloodstream and effectively accumulate in solid tumors after intravenous injection (8). The critical features of polymeric micelles for their function as drug vehicles, including size, drug loading and release, and specific binding to the target cells, can be modulated by engineering the

constituent block copolymers. At present, our micelle formulations incorporating doxorubicin, paclitaxel, SN-38, cisplatin, and (1,2-diaminocyclohexane) platinum(II) (DACHPt) are undergoing clinical trials (development code names NK911, NK105, NK102, NC-6004, and NC-4016, respectively), and four of these have advanced to Phase II studies (13–17). These clinical studies have revealed that polymeric micelles reduce side effects from the incorporated drugs and are effective against various intractable tumors, such as triple-negative breast cancers (18), indicating their clinical potential.

Recently, increasing attention has been paid to another potentially useful property of nanocarriers: to achieve subcellular drug targeting. Subcellular drug targeting of nanocarriers could enhance the pharmacological activity of the loaded drugs through improved subcellular drug distribution (19). Drug vehicles designed to release active drugs in acidic organelles, such as the endosome and lysosome, can circumvent recognition by the drug efflux pump (for example, P-glycoprotein) through internalization by endocytosis, thus overcoming multidrug resistance in cancer cells (20–22). Here, we aimed to investigate the potential of DACHPt-loaded micelles (DACHPt/m) for *in vivo* subcellular targeting. DACHPt/m is formed by the polymer-metal complexation between DACHPt and the carboxylic group of poly(ethylene glycol)-*b*-poly(glutamic acid) [PEG-*b*-P(Glu)] copolymers. DACHPt is the parent complex of the clinically approved drug oxaliplatin. Oxaliplatin has a hydrolyzable oxalate group to increase its solubility in water, which can be removed by nucleophiles in biological media, such as chloride ions. Aqua complexes ($[(\text{DACH})\text{Pt}(\text{H}_2\text{O})\text{Cl}]^+$ or $[(\text{DACH})\text{Pt}(\text{H}_2\text{O})_2]^{2+}$) of DACHPt exhibit chemotherapeutic activity. DACHPt/m releases DACHPt and the micelle structure dissociates depending on the pH and chloride ion concentrations, a result of ligand substitution of the Pt(II) from the carboxylates in the micelle core with the chloride ions in the medium (Fig. 1A) (23, 24). Moreover, after DACHPt/m is internalized into cancer cells, it would be expected to be exposed to different pH and chloride ion concentrations during subcellular trafficking (25). We hypothesized that DACHPt/m would be selectively released in low-pH cellular compartments, bypassing

¹Department of Bioengineering, Graduate School of Engineering, University of Tokyo, 7-3-1 Hongo, Bunkyo-ku, Tokyo 113-8656, Japan. ²Center for NanoBio Integration, University of Tokyo, Tokyo 113-8656, Japan. ³Center for Disease Biology and Integrative Medicine, Graduate School of Medicine, University of Tokyo, Tokyo 113-0033, Japan. ⁴Department of Molecular Pathology, Graduate School of Medicine, University of Tokyo, Tokyo 113-0033, Japan. ⁵Division of Molecular Pharmacology, Cancer Chemotherapy Center, Japanese Foundation for Cancer Research, 3-10-6 Ariake, Koto-ku, Tokyo 135-8550, Japan. ⁶Department of Materials Engineering, Graduate School of Engineering, University of Tokyo, Tokyo 113-8656, Japan.

*To whom correspondence should be addressed. E-mail: nishiyama@bmw.t.u-tokyo.ac.jp (N.N.); kataoka@bmw.t.u-tokyo.ac.jp (K.K.)

cytoplasmic detoxification and thereby improving potency and efficacy (Fig. 1B). Indeed, we previously reported that cisplatin-loaded micelles, which are formed in the same manner as DACHPt/m, caused different gene expression patterns than did cisplatin alone because of their different internalization pathways and the facilitated drug release in endosomes and lysosomes (26). To test the above-mentioned hypothesis, we constructed fluorescent-labeled DACHPt/m (F-DACHPt/m) with a dual fluorescent-labeling method so that we could follow the intracellular localization and dissociation of the micelles by using *in vivo* confocal microscopy, and intravitaly evaluated the extravasation, penetration, cellular uptake, and subcellular fate of DACHPt/m in tumor tissues and their activity against human colorectal cancers.

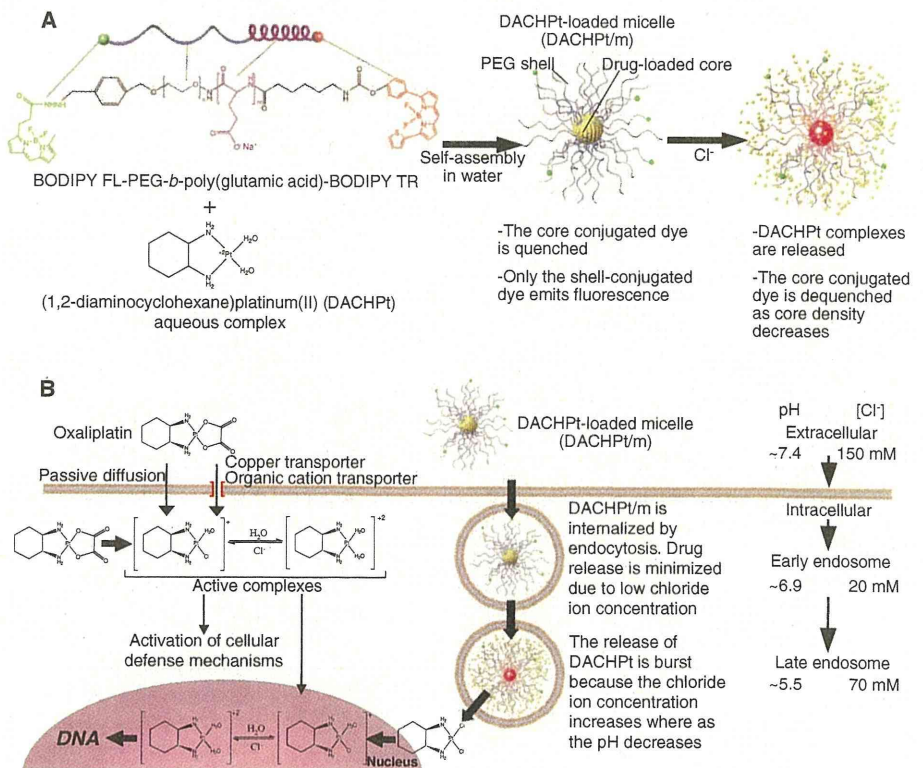
RESULTS

Construction and characterization of F-DACHPt/m

To construct the dual fluorescent-labeled block copolymer, we conjugated the fluorescent dyes boron dipyrromethene (BODIPY) FL (excitation wavelength, 503 nm; emission wavelength, 512 nm) and BODIPY TR (excitation wavelength, 588 nm; emission wavelength, 616 nm) to the α - and ω -end groups of α -4-(diethoxymethyl)benzyl-poly(ethylene glycol)-*b*-poly(L-glutamic acid), respectively, and thus obtained BODIPY FL-PEG-*b*-P(Glu)-BODIPY TR (fig. S1). The conjugation degree for BODIPY FL to the block copolymer was 0.2 mol BODIPY FL per mole of polymer and for BODIPY TR was about 0.8 mol BODIPY TR per mole of polymer. We built F-DACHPt/m by the formation of polymer-metal complexes between DACHPt and the carboxylic groups of

poly(glutamic acid) in BODIPY FL-PEG-*b*-P(Glu)-BODIPY TR (Fig. 1A). F-DACHPt/m had a diameter of 30 nm, similar to that of DACHPt/m (fig. S2). The intact F-DACHPt/m emitted fluorescence only from the shell-conjugated dye (BODIPY FL) because the core-conjugated dye (BODIPY TR) was quenched owing to its high local concentration. The close proximity of BODIPY TR fluorophores in the core of the micelles leads to self-quenching by the formation of nonfluorescent ground-state BODIPY TR dimers (or higher aggregates) (27). When DACHPt is released as a result of the ligand substitution of the Pt(II) from the carboxylates in the micelle core with the chloride in the medium, the density of the micelle core is reduced and the fluorescence of BODIPY TR is dequenched (Fig. 1A). We investigated the release of DACHPt from F-DACHPt/m and the fluorescence of BODIPY FL and BODIPY TR at the surface and core of the micelles, respectively, under conditions that mimicked the extracellular medium (pH 7.4 and 150 mM Cl⁻), early endosomes (pH 6.9 and 20 mM Cl⁻), and late endosomes and lysosomes (pH 5.5 and 70 mM Cl⁻) (25). The fluorescence from BODIPY FL on the shell of the micelles was constant regardless of the pH and salt concentration of the media (Fig. 2, A to C, middle columns), suggesting that the fluorescence from BODIPY FL can be used to trace the position of the micelles in the biological environment. In addition, the drug release profile of F-DACHPt/m was similar to that of unmodified DACHPt/m, suggesting the feasibility of a direct comparison (Fig. 2, A to C, left columns). Under extracellular conditions, BODIPY TR fluorescence increased after an incubation period of 17 hours, simultaneous with the release of DACHPt from F-DACHPt/m (Fig. 2A). The release of DACHPt from F-DACHPt/m in the late endosomal conditions was considerably faster (Fig. 2C) than in the extra-

Fig. 1. Design of fluorescent-labeled DACHPt/m (F-DACHPt/m) for visualization of the localization and drug release in the cell. (A) F-DACHPt/m self-assembled through polymer-metal complex formation between DACHPt and boron dipyrromethene (BODIPY) FL-poly(ethylene glycol)-*b*-poly(glutamic acid)-BODIPY TR in distilled water. In the micelle state, only BODIPY FL (green) emits fluorescence, whereas BODIPY TR (red) remains quenched. As DACHPt is released from F-DACHPt/m in chloride ion-containing media, BODIPY TR is dequenched and emits fluorescence. (B) Schematic representation of hypothetical subcellular pathways and action of DACHPt/m. Oxaliplatin enter cells by passive diffusion or through copper/organic cation transporters. Once oxaliplatin is in the cytoplasm, most of the activated aqua species ($[(DACH)Pt(H_2O)Cl]^+$ or $[(DACH)Pt(H_2O)_2]^{2+}$) are eliminated by cellular detoxification mechanisms, but a small fraction binds to DNA. In contrast, DACHPt/m that enters tumor cells by endocytosis (middle) is exposed to an environment with increasing acidity and chloride ion concentration because early endosomes mature into the late endosomes. Drug release from DACHPt/m is accelerated in the late endosomal environment close to the perinuclear region, resulting in enhanced efficiency of drug delivery to the nucleus.



cellular and early endosomal conditions (Fig. 2, A and B), occurring without any delay. Further, mirroring the DACHPt release, F-DACHPt/m exhibited more robust fluorescence recovery of BODIPY TR under the late endosomal conditions (Fig. 2C) than under the early endosomal conditions (Fig. 2B, right columns). Thus, the fluorescence profiles of BODIPY TR are correlated with the release profiles of DACHPt from the micelles.

In vitro subcellular trafficking of F-DACHPt/m

The cellular internalization and fate of F-DACHPt/m in human tumor-derived colorectal cancer (HT29) cells, which are the most frequently used cell lines in oxaliplatin studies (28), were observed with time-lapse confocal laser scanning microscopy (CLSM) (Fig. 3A and video S1). The intensity of BODIPY FL fluorescence increased slightly over time (Fig. 3B), and the BODIPY FL fluorescence in the images was clearly visible within a 6-hour incubation (Fig. 3A). Meanwhile, with time,

the intensity of BODIPY TR fluorescence continuously increased to a greater extent than did that of BODIPY FL fluorescence (Fig. 3B), and the BODIPY TR fluorescence in the images became visible at about 24 hours of incubation (Fig. 3A). This continuous increase in the intensity of BODIPY TR fluorescence corresponds to the dequenching of BODIPY TR fluorescence driven by the release of DACHPt in the cell. These results suggest that F-DACHPt/m enters the cells as a micelle form and then dissociates within the subcellular environments.

Using CLSM with higher magnification, we further evaluated the detailed subcellular trafficking and fate of F-DACHPt/m by focusing on individual cells. We confirmed that the micelles entered the cancer cells via endocytosis by incubating the cells with F-DACHPt/m at 37°C and 4°C. As endocytosis ceases at 4°C, the fluorescent signal of F-DACHPt/m inside the cells was undetectable, whereas at 37°C, the fluorescence from F-DACHPt/m was observed inside the cells (fig. S3). To examine the subcellular trafficking of the micelles, we determined the colocalization of BODIPY

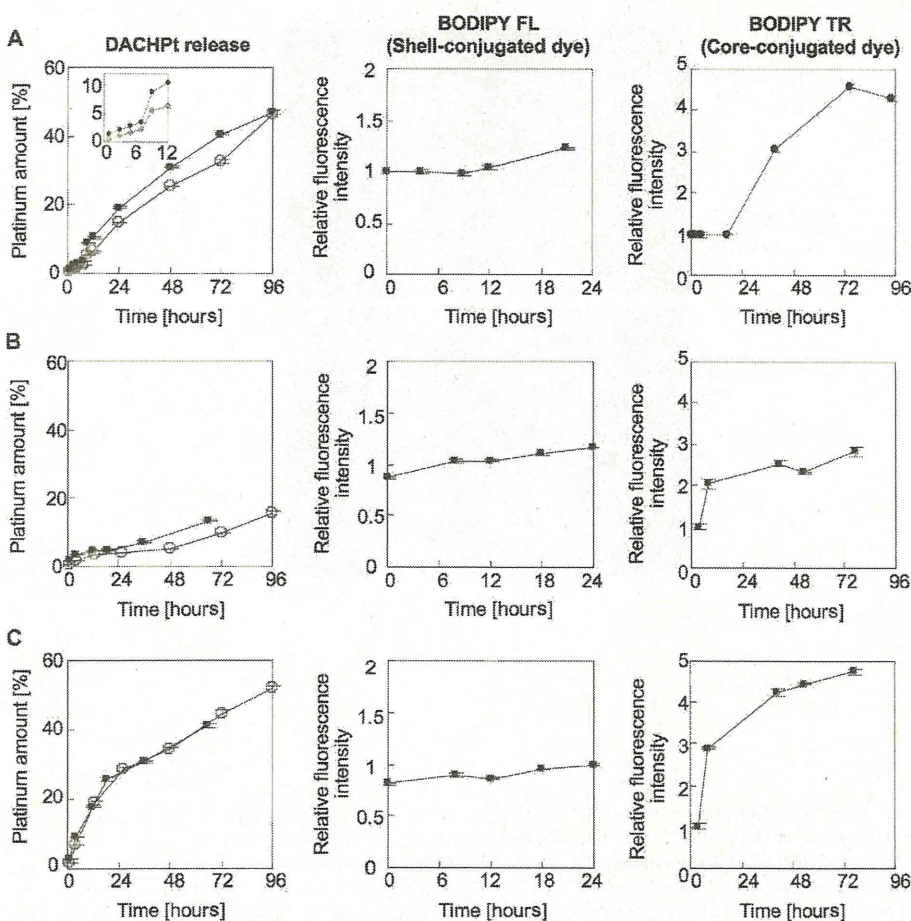


Fig. 2. Properties of F-DACHPt/m under conditions mimicking extracellular and subcellular environments. (A to C) Release profiles of DACHPt from DACHPt/m and F-DACHPt/m (left column) and fluorescence profiles of BODIPY FL (middle column) and BODIPY TR (right column) under conditions mimicking (A) the extracellular environment (10 mM PBS, pH 7.4, and 150 mM NaCl), (B) the early endosomal environment (10 mM PBS, pH 6.9, and 20 mM NaCl), and (C) the late endosomal environment (10 mM PBS, pH 5.5, and 70 mM NaCl), all at 37°C. Inset in top left panel is the magnification of the profiles of DACHPt release until 12 hours. The release of DACHPt from the micelles was evaluated by dialysis as described in Materials and Methods. Data for DACHPt/m and F-DACHPt/m in the left column are shown as open and filled circles, respectively. Data are expressed as means \pm SEM ($n = 3$).

FL fluorescence from F-DACHPt/m with an early endosome marker, Rab5a-RFP, and a late endosome and lysosome marker, LysoTracker, in HT29 cells (Fig. 3C). Note that individual vesicular organelles can be recognized as punctate fluorescence in the images. After a 6-hour incubation at 37°C, BODIPY FL colocalized mainly with Rab5a-RFP (yellow fluorescence in Fig. 3C, upper images) rather than with LysoTracker. After prolonged incubation (24 and 55 hours), BODIPY FL showed decreased colocalization with Rab5a-RFP and increased colocalization with LysoTracker (yellow fluorescence in Fig. 3C, lower images). This observation was confirmed by quantification of colocalized fluorescent intensities of BODIPY FL with Rab5a-RFP or LysoTracker (Fig. 3D). These results suggested that the micelles might localize mainly in the early endosome until 6 hours and then move into the late endosome/lysosome compartment. Furthermore, we studied the timing and location of the micelle dissociation and concomitant drug release by evaluating the colocalization of F-DACHPt/m with LysoTracker (Fig. 3E and fig. S4A) and the quantification of BODIPY FL and BODIPY TR fluorescent intensities (fig. S4B), as well as the colocalization ratio (Fig. 3F). The fluorescence intensity from BODIPY FL gradually increased (fig. S4B). Meanwhile, the fluorescence of BODIPY TR became visible after 24-hour incubation (Fig. 3E and fig. S4A) and then increased over time (fig. S4B). Both BODIPY FL and BODIPY TR colocalized with LysoTracker (Fig. 3E and fig. S4A), and the colocalization ratio between BODIPY FL or BODIPY TR and LysoTracker increased over time (Fig. 3F). These observations sug-

gested that F-DACHPt/m progressively dissociated in the late endosome and lysosomal compartments. Because these acidic organelles reside in the perinuclear region, F-DACHPt/m would be expected to deliver the active platinum complexes close to the nucleus. Thus, in vitro confocal microscopy revealed that F-DACHPt/m appears to exhibit late endosome/lysosome-selective dissociation concomitant with the release of DACHPt, thereby achieving efficient DACHPt delivery close to the nucleus.

Effect of subcellular pathway on drug efficiency

Oxaliplatin enters the cells by passive diffusion or through copper/organic cation transporters (29), and it then changes to active DACHPt aqua complexes in the cytoplasm, some of which may ultimately cross-link with DNA, disrupting DNA function and exerting therapeutic activity (Fig. 1B). However, 75 to 85% of activated platinum drugs are sequestered by abundant sulfur species that serve as cellular defense mechanisms in the cytoplasm, and only 5 to 10% of oxaliplatin can bind to DNA (Fig. 1B) (30–32). We hypothesized that DACHPt/m facilitates drug delivery close to the nucleus through its perinuclear subcellular localization. Therefore, we studied the pharmacological activity of DACHPt/m. DACHPt/m displayed a value of IC_{50} (the mean concentration that causes 50% growth inhibition) against HT29 cells that was lower than that of oxaliplatin by a factor of 4.7 (Table 1). It is rare that a nanocarrier-encapsulated drug surpasses the free form of the drug for in vitro cytotoxicity (33). To elucidate the mechanism of DACHPt/m action, we evaluated the subcellular accumulation of platinum and quantity of Pt-DNA adducts. Exposure of HT29 cells to oxaliplatin resulted in twice as much accumulation of platinum than did exposure to DACHPt/m (Fig. 3G). This is probably because oxaliplatin rapidly enters the cells by diffusion and through copper/organic cation transporters (29), whereas DACHPt/m is gradually internalized by endocytosis. Nevertheless, we did not observe a significant difference in the Pt-DNA adducts formed after exposure to oxaliplatin and DACHPt/m (Fig. 3H), indicating that DACHPt/m may efficiently deliver the active platinum drug to DNA (Fig. 3I).

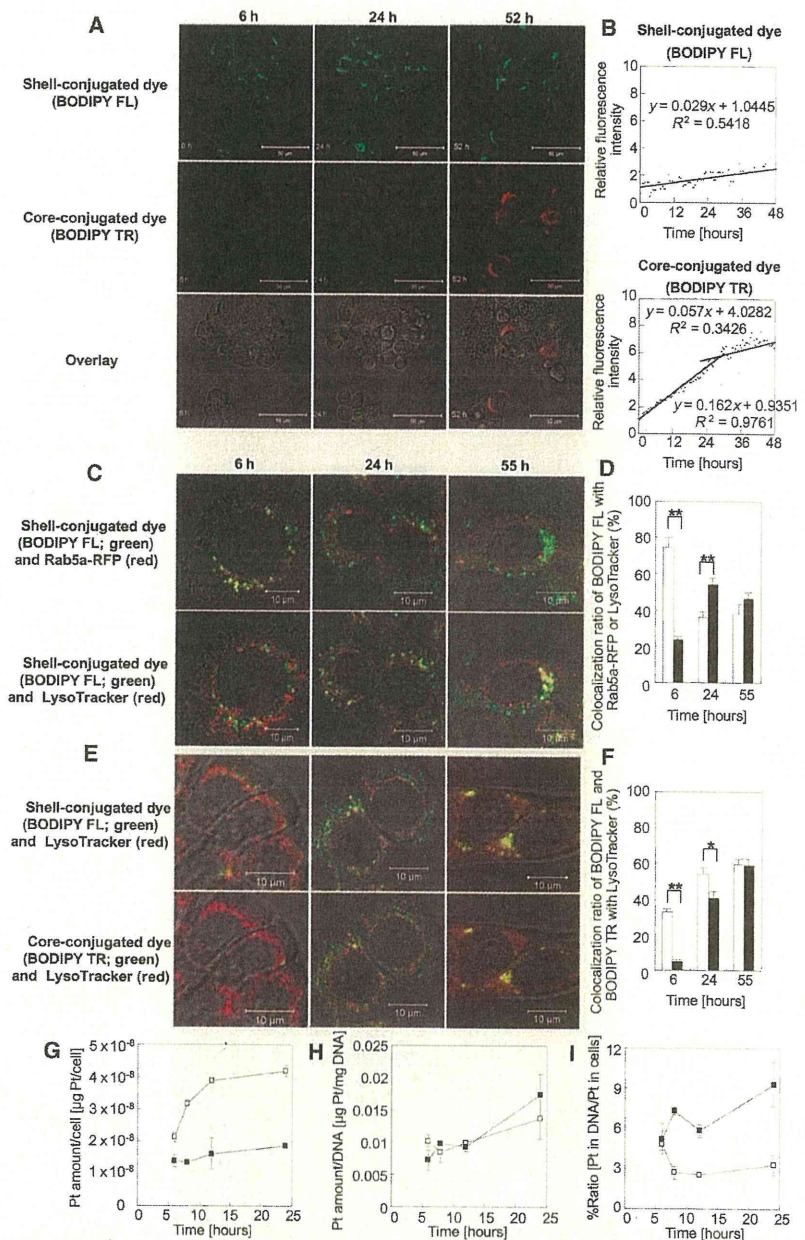


Fig. 3. In vitro observation of subcellular trafficking and fate of F-DACHPt/m, cellular platinum accumulation, and formation of platinum-DNA adducts. (A) Representative images of time-lapse CLSM observation of HT29 cells treated with F-DACHPt/m (green, BODIPY FL; red, BODIPY TR; yellow, their colocalization). (B) Relative fluorescence intensity of BODIPY FL (upper) and BODIPY TR (lower) of F-DACHPt/m. (C) Fluorescent images of colocalization of BODIPY FL of DACHPt/m (green) with an early endosome marker, Rab5a-RFP (red in upper images), or a late endosome and lysosome marker, LysoTracker (red in lower images), in HT29 cells after incubation for 6, 24, and 55 hours. (D) Colocalization ratio of BODIPY FL with Rab5a-RFP (open bars) or LysoTracker (closed bars). Data are expressed as means \pm SEM ($n = 10$). $**P < 0.01$. (E) Fluorescent images of colocalization of BODIPY FL (green in upper images) and BODIPY TR (green in lower images) of F-DACHPt/m with LysoTracker (red) in HT29 cells after incubation for 6, 24, and 55 hours. (F) Colocalization ratio of BODIPY FL (open bars) or BODIPY TR (closed bars) with LysoTracker. Data are expressed as means \pm SEM ($n = 10$). $*P < 0.05$; $**P < 0.01$. (G) In vitro cellular accumulation of platinum. (H) DNA platination. (I) Ratio of platinum in DNA to total platinum in cells expressed as a percentage. DNA platination was converted from $\mu\text{g Pt}/\text{mg DNA}$ to $\mu\text{g Pt}/\text{cell}$, and the ratio was calculated. Open squares, oxaliplatin; filled squares, DACHPt/m. Data are expressed as means \pm SEM ($n = 3$).

We also evaluated the mean concentration required for 50% growth inhibition (GI_{50}), which is defined as in (34, 35), in a human cell panel composed of 37 cancer cell lines (fig. S5), and investigated the correlation between GI_{50} and expression of 26 genes that we selected on the basis of their potential association with the pharmacological activity of platinum compounds (36). The cytotoxic activity of oxaliplatin was inversely correlated with the expression of metallothionein (MT1Q) and methionine synthase (MTR), which are found in the cytoplasm and inactivate platinum compounds. DACHPt/m cytotoxicity did not exhibit similar correlations (table S1). We conclude that DACHPt/m may bypass cytoplasmic detoxification by MTR and MT1Q and efficiently deliver active platinum complexes to the nucleus, because they are internalized by endocytosis and selectively release the active platinum complexes in the late endosome/lysosome compartment (Fig. 1B).

Effect of DACHPt/m on oxaliplatin resistance in vitro

Our proposed mechanism of action of DACHPt/m led us to investigate their efficacy in oxaliplatin-resistant cancer cells, because MTR and MT1Q are overexpressed in these cells (37–39). We developed oxaliplatin-resistant HT29 cells (HT29/ox) by chronic exposure of HT29 cells to oxaliplatin with gradual dose escalation. Relative to the parental HT29 cells, HT29/ox cells were 10 times as resistant to oxaliplatin (Table 1). Quantitative real-time reverse transcription polymerase chain reaction (RT-PCR) and Western blotting revealed that the HT29/ox cells showed up-regulated messenger RNA (mRNA) as well as protein for MTR and MT1Q compared with HT29 cells (Fig. 4, A and B). Moreover, the down-regulation of MT1Q and MTR with small interfering RNA (siRNA) restored the sensitivity of HT29/ox cells to oxaliplatin (fig. S6). In vitro cytotoxicity studies showed that DACHPt/m was 120 times as cytotoxic as oxaliplatin in HT29/ox cells (Table 1). These results suggested that DACHPt/m may overcome acquired resistance to oxaliplatin.

In vivo intratumoral imaging of F-DACHPt/m in a human colon cancer model

DACHPt/m would need to extravasate, penetrate into the interstitial tissue, and be internalized by cancer cells after systemic administration to exert the in vivo antitumor activity predicted from the results above. We performed real-time intravital observation of the accumulation and subcellular fate of F-DACHPt/m in HT29 xenografts by using in vivo CLSM equipped with a high-speed resonant scanner developed to acquire live tissue images of experimental animals (fig. S7). Immediately after intravenous injection, F-DACHPt/m was observed in the blood vessels of solid tumors (Fig. 5A and video S2). The fluorescence from F-DACHPt/m in the blood vessels corresponded only to that of BODIPY

FL. Even 12 hours later, only BODIPY FL fluorescence was observed flowing in the blood vessels (Fig. 5B and video S3). These observations indicate that F-DACHPt/m stably circulates in the bloodstream while maintaining their micellar structure. Images of tumor tissue revealed the accumulation and dissociation behaviors of F-DACHPt/m (Fig. 5, C and D, and video S3). Two hours after injection, F-DACHPt/m accumulated within the tumor tissue because of the EPR effect and was identified within the cells, whereas BODIPY TR fluorescence remained quenched. BODIPY TR fluorescence gradually appeared inside the cells 4 hours after injection and was clearly visible after 12 hours, indicating the release of DACHPt

Table 1. In vitro cytotoxicity of free oxaliplatin and DACHPt/m against HT29 and HT29/ox cells after a 48-hour incubation. Data are expressed as means \pm SEM ($n = 4$).

Cells	IC_{50} (μ M)*		
	Free oxaliplatin	DACHPt/m	Oxaliplatin/DACHPt/m
HT29	2.2 \pm 2.2	0.47 \pm 0.05	4.7
HT29/ox	22.8 \pm 2.6	0.19 \pm 0.11	120
Ratio of HT29/ox/HT29	10.4	0.4	—

* IC_{50} values obtained from the MTT assay.

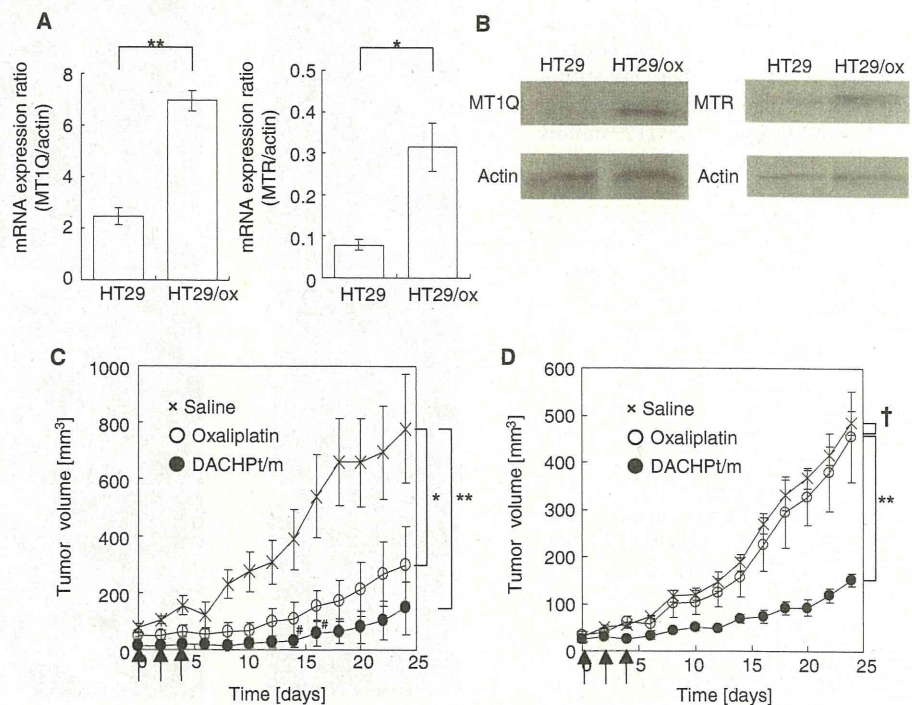


Fig. 4. Expression of MT1Q and MTR in HT29/ox cells and effects of DACHPt/m on HT29 and HT29/ox tumors in vivo. (A) Relative mRNA expression of metallothionein (MT1Q) and methionine synthase (MTR) in parent HT29 and HT29/ox cell lines. Data are expressed as means \pm SEM ($n = 3$). * $P < 0.05$; ** $P < 0.01$. (B) Western blots of MT1Q and MTR in HT29 and HT29/ox cell lines. (C and D) In vivo effect of DACHPt/m on subcutaneous HT29 (C) and HT29/ox (D) tumor cells. Crosses, saline; open circles, oxaliplatin (8 mg/kg); filled circles, DACHPt/m (4 mg/kg); arrows, injection of oxaliplatin and DACHPt/m; #, tumor regression; † $P > 0.1$; * $P < 0.05$; ** $P < 0.01$. Data are expressed as means \pm SEM ($n = 4$).

from the micelles inside the cells in the tumor tissue. The cell membrane, stained with CellMask, and cell nuclei were substantially free of F-DACHPt/m (Fig. 5, C and D, and video S3). These results were consistent with our *in vitro* results (Fig. 3A) and suggested that F-DACHPt/m percolated into interstitial tissues and was efficiently internalized to endosomal compartments of cells in a micelle form, followed by dissociation of the multimolecular structure of the micelles in the late endosomal and lysosomal compartments.

DACHPt/m enhances antitumor activity and overcomes oxaliplatin resistance *in vivo*

On the basis of our observations of the *in vivo* behavior of F-DACHPt/m, we hypothesized that DACHPt/m may also overcome oxaliplatin resistance *in vivo*. Thus, we evaluated DACHPt/m *in vivo* antitumor activity against subcutaneous HT29 and HT29/ox tumors (Fig. 4, C and D). Although free oxaliplatin failed to inhibit the growth of HT29/ox tumors, DACHPt/m exhibited substantial antitumor activity in the oxaliplatin-resistant xenograft model and successfully overcame the oxaliplatin resistance of HT29/ox cells *in vivo* (Fig. 4D). Note that DACHPt/m also achieved higher antitumor activity than oxaliplatin against the HT29 tumors (Fig. 4C). Thus, our micelle-based drug delivery vehicle was able to circumvent the detoxification mechanisms against platinum drugs in tumor cell cytoplasm through selective subcellular drug release and hence overcome acquired resistance.

DISCUSSION

Colorectal cancer is a major cause of morbidity and mortality worldwide (1). Oxaliplatin is currently the standard therapy for colorectal cancer, and acquired resistance to oxaliplatin is a major clinical drawback in the treatment of colorectal cancer [virtually all metastatic colorectal cancer becomes resistant to oxaliplatin, with a median time to progression of 8.7 months (40)]. The major cellular processes by which oxaliplatin enters and attacks cancer cells include uptake and transport, formation of DNA adducts and their recognition by damage response proteins, and signal transduction leading to apoptosis. Any factors that interfere with these pathways can lead to drug resistance (41). Here, we showed

that DACHPt/m can overcome drug resistance by circumventing recognition by MTR and MT1Q, and achieve subcellular drug delivery both *in vitro* and *in vivo* to the perinuclear region of cells. It has been reported that drug delivery systems can overcome multidrug resistance

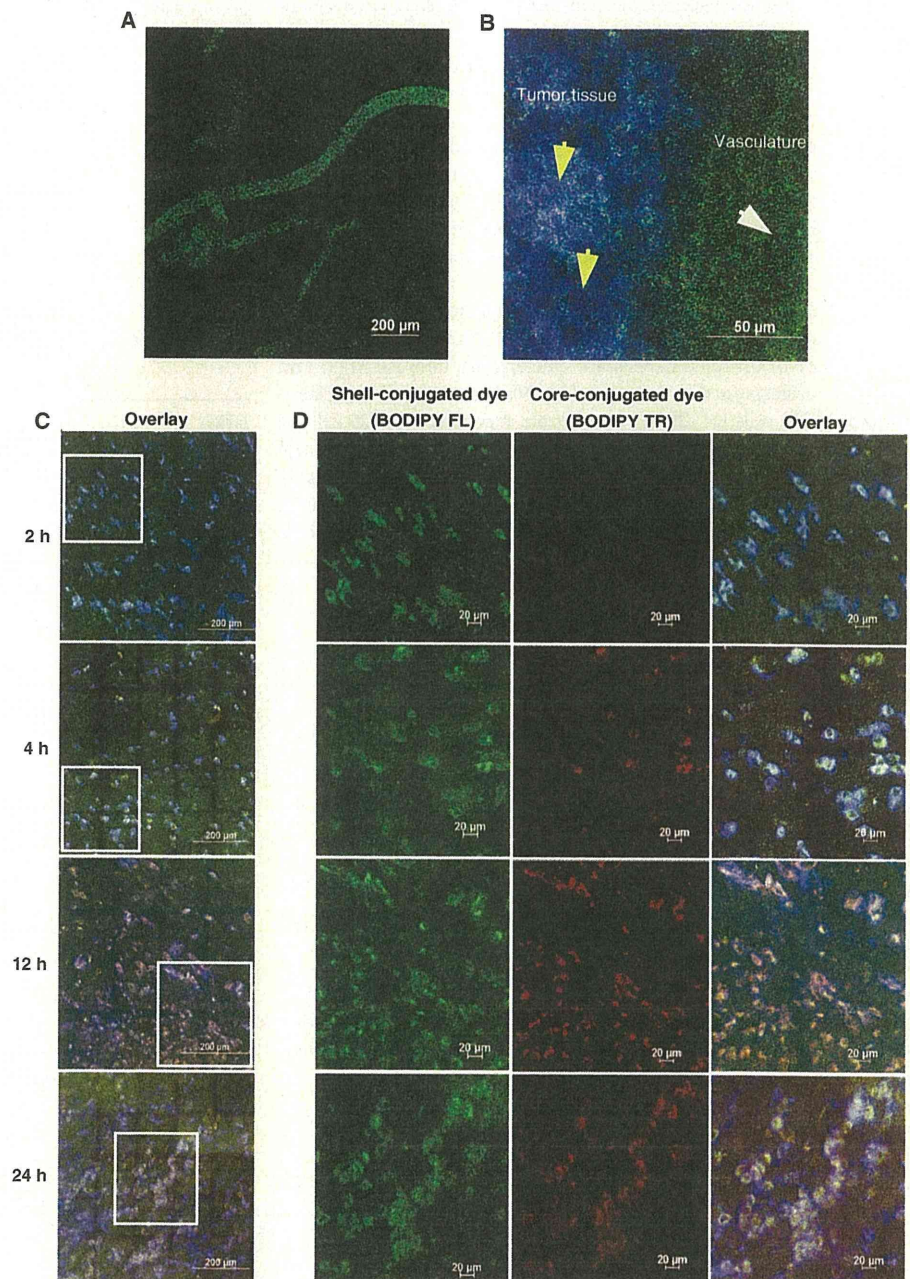


Fig. 5. *In vivo* CLSM observation of F-DACHPt/m in blood vessels and tumors after intravenous administration. (A and B) CLSM observation of F-DACHPt/m in the blood vessels of solid tumors (A) immediately after injection and (B) in the tumor tissue at 12 hours after injection. Yellow arrows, tumor tissue; white arrow, blood vessel. (C) Time-dependent CLSM observation of F-DACHPt/m in the tumor tissues at 2, 4, 12, and 24 hours after injection. Green, fluorescence from the shell-conjugated dyes (BODIPY FL); red, core-conjugated dyes (BODIPY TR); blue, cell surfaces stained by CellMask. (D) Magnification of selected areas [square regions in (C)] by channel.

by avoiding the drug efflux mechanism of P-glycoprotein (20–22). Because P-glycoprotein is not associated with platinum drug resistance (42), we used a different approach. Our data indicate that cytoplasmic detoxification mechanisms against platinum drugs can potentially be avoided by using the appropriate drug delivery system.

Nanocarriers encounter numerous barriers *in vivo* en route to their target during the processes of blood circulation, extravasation, penetration, and cellular uptake. It is therefore difficult to extrapolate *in vivo* outcomes of a drug-nanocarrier combination from its *in vitro* behavior, although real-time observation of *in vivo* behaviors such as we have used here can ascertain critical barriers residing in a living body and facilitate the design of a nanocarrier optimized for *in vivo* delivery. The *in vivo* CLSM technique that we used in this study enabled spatiotemporal and quantitative analyses of extravasation, tissue penetration, and cellular internalization of nanocarriers in living animals. Using dual fluorescent labeling of DACHPt/m, we elucidated the real-time intratumoral behavior of DACHPt/m. The dual fluorescent label of DACHPt micelles allowed us to trace the micelles' position by the ever-present fluorescent signal from the surface of the micelles, and the drug release and dissociation of the multimolecular structure of the micelles by the quenching and fluorescence recovery of the core-conjugated dye. In *in vitro* cellular experiments, these micelles were internalized intact, and then they were disassembled and the drug was released in late endosomes. In our *in vivo* microscopy, we observed that DACHPt/m maintained their micelle form during circulation in the blood, probably because of the stable inner core structure formed by the polymer-metal complexes, and extravasated into solid tumors. DACHPt/m was able to deeply penetrate cancerous tissue after extravasation and was internalized by different cell populations that were distant from the blood vessels. Such efficient penetration of tissue is a requirement of successful drug delivery and a prerequisite for effective subcellular targeting. It has been reported that PEG-modified liposomes with 100-nm diameter accumulated at perivascular regions of solid tumors and failed to penetrate the tumor interstitium deeply (43). Although this characteristic may depend on the cancer type, it is possible that the deep tumor penetration of DACHPt/m is a result of their smaller 30-nm size. Finally, the DACHPt/m structure dissociated at the perinuclear regions of the cell after internalization, based on the pH and chloride ion concentration-selective release of DACHPt. This observation is also consistent with our hypothesis that DACHPt/m can overcome oxaliplatin resistance in tumors by bypassing the cytoplasmic detoxification mechanisms of MTR and MT1Q. There are, however, several limitations to the type of study that we have performed in a subcutaneous tumor model. Compared with subcutaneous tumors, orthotopic and spontaneously forming tumors may have characteristic differences such as vascular density and degree of fibrosis, which may affect the transport of nanocarriers (44).

Our research provides one approach for subcellular targeting of cytoplasmic drugs. Such nanocarriers have the potential to enhance the drug efficacy and overcome drug resistance.

MATERIALS AND METHODS

Materials

γ -Benzyl L-glutamate and bis(trichloromethyl) carbonate (triphosgene) were purchased from Sigma Chemical and Tokyo Kasei Kogyo, respec-

tively. *N,N*-Dimethylformamide (DMF), 3-(4,5-dimethylthiazol-2-yl)-2,5-diphenyltetrazolium bromide (MTT), and dimethyl sulfoxide (DMSO) were purchased from Wako Pure Chemicals. Oxaliplatin and NaCH₃CN were purchased from Sigma-Aldrich Inc. Dichloro(1,2-diammino cyclohexane) platinum(II) was purchased from W. C. Heraeus GmbH. α -Methoxy- ω -amino-poly(ethylene glycol) [CH₃O-PEG-NH₂; molecular weight (MW), 12,000] was purchased from Nippon Oil and Fats. BODIPY TR-succinimidyl ester, BODIPY FL-hydrazide, LysoTracker Blue, CellLight Early Endosome-RFP (Rab5a-RFP), CellMask, and Lipofectamine RNAiMAX were purchased from Invitrogen.

Cell lines and animals

HT29 cells were purchased from the American Type Culture Collection. HT29 cells were maintained in McCoy's 5A modified medium (Invitrogen) containing 10% fetal bovine serum (Gibco) as well as 1% penicillin and streptomycin (Sigma) and were cultured at 37°C in a humidified atmosphere of 5% CO₂. To develop HT29/ox cells (45), we treated HT29 cells with oxaliplatin at IC₅₀ doses for 1 hour. After 24 hours, cells were subcultured into new flasks and oxaliplatin was added to a culture of 80% confluent cells. The concentration was incrementally increased by factors of 1.2 to 2. The process was continued until the cells were resistant to drug concentrations at least 10 times as great. BALB/c-nu/nu mice (female; body weight, 18 to 20 g; age, 6 weeks old) were purchased from Charles River Japan. All animal experiments were carried out in accordance with the guidelines for animal experiments at the University of Tokyo, Japan.

Methods

Synthesis of block copolymers. α -4-(Diethoxymethyl)benzyl- ω -amino-poly(ethylene glycol) (Ac-Bz-PEG-NH₂) was previously synthesized in our laboratory (46). Poly(ethylene glycol)-*b*-poly(L-glutamic acid) [PEG-*b*-P(Glu)] [MW_{PEG}, 12,000; polymerization degree of P(Glu), 20] and Ac-Bz-PEG-*b*-poly(L-glutamic acid) [Ac-Bz-PEG-*b*-P(Glu)] [MW_{PEG}, 12,000; polymerization degree of P(Glu), 20] were synthesized according to the previously described synthetic method (47). Briefly, *N*-carboxyanhydride of γ -benzyl L-glutamate (BLG-NCA) was synthesized by the Fuchs-Farthing method with triphosgene (48). BLG-NCA was polymerized in DMF initiated by the amino group of CH₃O-PEG-NH₂ or Ac-Bz-PEG-NH₂ to obtain PEG-*b*-poly(γ -benzyl L-glutamate) (PEG-*b*-PBLG) or Ac-Bz-PEG-*b*-PBLG, respectively. The MW distribution of PEG-*b*-PBLG and Ac-Bz-PEG-*b*-PBLG was determined by gel permeation chromatography (GPC) [column, TSK-gel G3000HHR, G4000HHR (Tosoh); eluent, DMF containing 10 mM LiCl; flow rate, 0.8 ml/min; detector, refractive index; temperature, 25°C]. PEG-*b*-PBLG and Ac-Bz-PEG-*b*-PBLG showed narrow MW distributions (M_w/M_n : 1.09 and 1.16, respectively) in GPC. The degrees of polymerization of PBLG in PEG-*b*-PBLG and Ac-Bz-PEG-*b*-PBLG were determined to be 20 by comparing the proton ratios of methylene units in PEG (-OCH₂CH₂-; δ = 3.7 ppm) and phenyl groups of PBLG (-CH₂C₆H₅; δ = 7.3 ppm) in ¹H-NMR (nuclear magnetic resonance) measurement. Both PEG-*b*-PBLG and Ac-Bz-PEG-*b*-PBLG were deprotected by mixing with 0.5 N NaOH at room temperature to obtain PEG-*b*-P(Glu) and Ac-Bz-PEG-*b*-P(Glu), respectively. Complete deprotection was confirmed by ¹H NMR measurement.

Preparation of micelles. For conjugation of BODIPY TR to a polymer, a solution of BODIPY TR-succinimidyl ester in DMSO (1 mg/ml) was mixed with Ac-Bz-PEG-*b*-P(Glu). The reaction was carried out overnight at room temperature with stirring. Unreacted

BODIPY TR was removed by dialysis [MW cutoff (MWCO) size, 2000 daltons] against DMSO and water. To conjugate BODIPY FL to the Ac-Bz-PEG-*b*-P(Glu)-BODIPY TR polymer, we mixed a solution of BODIPY FL-hydrazide in DMSO with the polymer, followed by the addition of 1 N HCl to deprotect the acetal group. Samples were stirred overnight at room temperature and treated with NaBH₃CN to reduce the link between BODIPY FL and the polymer. For purification, unbound BODIPY FL was removed by dialysis (MWCO, 2000 daltons) against DMSO and water. The prepared BODIPY FL-PEG-*b*-P(Glu)-BODIPY TR copolymer was freeze-dried overnight and stored at -20°C. DACHPt/m and F-DACHPt/m were prepared according to the previously described method (23). DACHPt (5 mM) was suspended in distilled water and mixed with silver nitrate ([AgNO₃]/[DACHPt] = 1) to form aqueous complexes. The solution was kept in the dark at 25°C for 24 hours. AgCl precipitates were eliminated by centrifugation. The supernatant was purified by passage through a 0.22- μ m filter. DACHPt aqueous complex solution was then mixed with PEG-*b*-P(Glu) or BODIPY FL-PEG-*b*-P(Glu)-BODIPY TR ([Glu] = 5 mM; [DACHPt]/[Glu] = 1.0) and reacted for 120 hours to obtain DACHPt/m or F-DACHPt/m, respectively. DACHPt/m and F-DACHPt/m were purified by ultrafiltration (MWCO, 30,000 daltons; Fig. 1A). The size distributions of DACHPt/m and F-DACHPt/m were evaluated by dynamic light scattering at 25°C with a Zetasizer Nano ZS90 (Malvern Instruments). The platinum content of DACHPt/m was determined by ion-coupled plasma mass spectrometry (4500 ICP-MS; Hewlett Packard).

Drug release and fluorescence profiles of micelles under different conditions. The release of platinum from DACHPt/m and F-DACHPt/m in phosphate-buffered saline (PBS) at 37°C was evaluated as described (23). Briefly, a micelle solution of known platinum concentration was placed inside a dialysis bag (MWCO, 2000 daltons). The solution was then dialyzed against PBS under different conditions mimicking the extracellular environment (10 mM PBS, pH 7.4, and 150 mM NaCl), early endosomes (10 mM PBS, pH 6.9, and 20 mM NaCl), and late endosomes (10 mM PBS, pH 5.5, and 70 mM NaCl) at 37°C (25). The concentration of platinum present in the dialysate was determined with ICP-MS. The fluorescence profiles of F-DACHPt/m were also evaluated under the same conditions with a spectrofluorometer (FP6600, Jasco) or NanoDrop (ND3300, Scrum). Changes in fluorescence intensity were measured at a defined time period.

In vitro observation of subcellular localization and the fate of F-DACHPt/m by CLSM. HT29 cells were cultured at 1×10^5 cells in 35-mm glass-based dishes (Asahi Techno Glass). After overnight incubation in a fresh medium, the cells were washed twice with PBS. The medium was then replaced by 1 ml of fresh medium containing F-DACHPt/m (100 μ M on Pt base). Live-cell CLSM imaging was performed with a Zeiss LSM 510 META nonlinear optics scan head attached to an inverted Axiovert 200 M SP equipped with a 63×1.4 numerical aperture Plan Aplanachromat oil immersion objective (Carl Zeiss). For long-term time-lapse imaging, culture dishes were wrapped with an optically clear foil cover (Carl Zeiss) to avoid evaporation and mounted onto the microscope stage incubator (37°C, 5% CO₂, 90% relative humidity). Bright-field DIC (differential interference contrast) images and fluorescent sequences were taken every 30 min for 72 hours. BODIPY FL was excited at 488 nm with an Ar laser and fluorescence was detected at 500 to 530 nm, whereas BODIPY TR was excited at 543 nm with a He-Ne laser, and fluorescence was detected at 565 to 615 nm. Laser power was kept low at 0.36 mW for 488 nm and

at 0.018 mW for 543 nm so that photobleaching was negligible. To determine whether DACHPt/m was taken up by endocytosis, we treated HT29 cells with F-DACHPt/m at 37°C or 4°C for 6 hours and then observed by CLSM. For the colocalization studies, we used micelles prepared from BODIPY FL-PEG-P(Glu) that only emit fluorescence from the shell. HT29 cells, which had been preincubated with CellLight Early Endosome-RFP to express an early endosome marker, Rab5a-RFP, were treated with BODIPY FL-conjugated DACHPt/m, and images were taken at indicated time points after staining with LysoTracker Blue. Rab5a-RFP was excited at 543 nm with a He-Ne laser, and fluorescence was detected at 565 to 615 nm. LysoTracker Blue was excited in multiphoton mode at 710 nm with a Mai Tai tunable broadband laser (Spectra-Physics), and fluorescence was detected at 390 to 465 nm. Colocalization was quantified as follows:

$$\begin{aligned} \text{amount of colocalization (\%)} \\ = \text{BODIPY FL pixels}_{\text{colocalization}} / \text{BODIPY FL pixels}_{\text{total}} \times 100 \end{aligned}$$

where BODIPY FL pixels_{colocalization} represents the number of BODIPY FL pixels colocalizing with Rab5a-RFP or LysoTracker pixels in the cytoplasm, and BODIPY FL pixels_{total} represents the number of all BODIPY FL pixels in the cytoplasm. The timing and location of the micelle dissociation and concomitant drug release were studied by evaluating the colocalization of BODIPY FL and BODIPY TR signals from F-DACHPt/m with the late endosomes/lysosomes (Fig. 3, E and F). Cells were treated with F-DACHPt/m, and images were taken at indicated time points after staining with LysoTracker Blue. Colocalization was quantified as follows:

$$\begin{aligned} \text{amount of colocalization (\%)} \\ = \text{BODIPY FL or BODIPY TR pixels}_{\text{colocalization}} / \text{BODIPY} \\ \text{FL or BODIPY TR pixels}_{\text{total}} \times 100 \end{aligned}$$

where BODIPY FL or BODIPY TR pixels_{colocalization} represents the number of BODIPY FL or BODIPY TR pixels colocalizing with LysoTracker pixels in the cytoplasm, and BODIPY FL or BODIPY TR pixels_{total} represents the number of all BODIPY FL or BODIPY TR pixels in the cytoplasm.

Determination of subcellular Pt accumulation and amount of Pt-DNA adducts. HT29 cells (6×10^6) were seeded in 100-mm tissue culture dishes. After 24 hours, cells were treated with 10 μ M oxaliplatin or DACHPt/m on a platinum base. After 6, 8, 12, and 24 hours of drug exposure, the medium was removed and the cells were washed three times with PBS, scraped, and harvested. Samples were freeze-dried overnight, dissolved in heated nitric acid, and evaporated to dryness. The samples were redissolved in water and the Pt content was determined by ICP-MS. For the quantification of Pt-DNA adducts, DNA was extracted with a DNA purification kit (Promega) according to the manufacturer's protocol. The amount and purity of DNA were determined by measuring absorption at 260 and 280 nm with NanoDrop (ND3300). The DNA was dissolved in nitric acid, dried, and redissolved in water. The Pt content was determined by ICP-MS, and the DNA platination levels were expressed as micrograms of Pt per milligram of DNA.

In vitro cytotoxicity study against human cancer cells. The in vitro cytotoxicity of oxaliplatin and DACHPt/m was examined against a panel of 37 human cancer cells as described (34, 35). Cancer cells were plated into flat-bottomed 96-well plates at 5×10^3 per well. Cells were treated by continuous exposure to oxaliplatin or DACHPt/m in a final volume of 100 μ l. Plates were incubated for 48 hours at 37°C in a humidified atmosphere with 5% CO₂, and cell viability was determined

by MTT assay. To determine the relationship between cellular sensitivity to oxaliplatin or DACHPt/m and the expression of genes involved in the sensitivity or resistance of cells to platinum compounds, we assessed the gene expression profile of 21 human cancer cell lines for 26 genes selected on the basis of previous studies on cisplatin- or oxaliplatin-resistant cells (36). Expression of these individual genes was determined by searching the National Cancer Institute database. The coefficient of correlation between the GI₅₀s of free oxaliplatin and DACHPt/m as well as the level of gene expression was calculated for each gene.

Quantitative real-time RT-PCR. The expression of the metallothionein (MT1Q) [human MT1B (same as MT1Q), NM_005947, 4MQ-012725-01-0002] and methionine synthase (MTR) (human MTR, NM_000254, 4LQ-009896-00-0002) was confirmed by quantitative real-time RT-PCR. After 24 hours of treatment, cells were washed with PBS and harvested. Total RNA was prepared with TRIzol (Invitrogen), and complementary DNA (cDNA) was reverse-transcribed with a QuantiTect reverse transcription kit (Qiagen). PCR primer sequences were as follows: MT1Q, 5'-GAACTCCAGGCTTGCTTGG-3' (forward) and 5'-CATTTGCACTCTTTCACCTG-3' (reverse); MTR, 5'-ACCCAATTCCAGGGAGACT-3' (forward) and 5'-GGCACATGATCTTGGACTT-3' (reverse); actin, 5'-AGATGTGGATCAGCAAGCAG-3' (forward) and 5'-GCGCAAGTTAGGTTTTGTCA-3' (reverse); and 18S, 5'-CGGCGACGACCCATTCGAAC-3' (forward) and 5'-GAATCGAACCTGATTCCCCGTC-3' (reverse). cDNA from HT29 cells was amplified with specific primers with a SYBR Green Core Reagent Kit (Qiagen) and a real-time PCR instrument (Applied Biosystems). Expression of each gene was standardized with endogenous actin or 18S as a control, and its relative levels in HT29 or HT29/ox cells were quantified by calculating $2^{-\Delta\Delta C_T}$, where $\Delta\Delta C_T$ is the difference in C_T (cycle number at which the amount of amplified target reaches a fixed threshold) between target and reference.

MT1Q and MTR gene knockdown. The siRNAs against MT1Q and MTR and the control siRNA were purchased from Thermo Fisher Scientific Inc. The siRNA target sequences against MT1Q are the following: siMT1Q, GCAAAGGCUCAUCAGAGAA. The siRNA sequences against MTR are the following: siMTR, CUGAGAAGCUCUUACGUUA. The siRNAs were transfected into the cell with Lipofectamine RNAiMAX (Invitrogen) according to the instructions of the manufacturer. Briefly, HT29/ox cells (4×10^5) were seeded in six-well plates. Twenty-four hours later, the mixture of siMT1Q (50 nM) and siMTR (50 nM) was transfected into the cells with Lipofectamine RNAiMAX reagent. Knockdown of MT1Q and MTR was separately confirmed by real-time PCR (fig. S6, A and B, respectively). To investigate the role of MT1Q and MTR in the oxaliplatin resistance in HT29/ox cells, we seeded HT29/ox cells (5×10^3) in 96-well plates, and 24 hours later, the mixture of siMT1Q (50 nM) and siMTR (50 nM) or the control siRNA was transfected into the cells with Lipofectamine RNAiMAX reagent. Twenty-four hours after transfection, the transfected HT29/ox cells were treated by continuous exposure to oxaliplatin in a final volume of 100 μ l. Plates were further incubated for 48 hours at 37°C in a humidified atmosphere with 5% CO₂, and their cytotoxicity was determined by MTT assay.

Western blotting. HT29 or HT29/ox cells (5×10^6) were seeded in 100-mm² plates and washed with PBS (100 μ l). Cell extracts were resolved in TNE buffer [1% NP-40, 150 mM NaCl, 10 mM tris-HCl, 1 mM EDTA, aprotinin (10 μ g/ml), 2 mM Na₃VO₄, 10 mM NaF]. The cell suspension was centrifuged for 20 min at 15,000g. Sampling buffer (4 \times) was added to the aliquots, followed by incubation

for 5 min at 100°C. Transfer to a polyvinylidene difluoride membrane (Invitrogen) was performed by electrophoresis for 90 min at 125 V. Membranes were blocked with 6% nonfat milk or tris-buffered saline (TBS) with 0.1% Tween 20 (MT1Q) for 1 hour. They were then probed at room temperature with the following antibodies: anti-metallothionein (ab12228, 1:1000, Abcam), anti-methionine synthase (ab66039, 1:2000, Abcam), and anti- β -actin (#4967, 1:1000, Cell Signaling). Membranes were washed three times with washing buffer (TBS with 0.1% Tween 20) and then probed with the secondary anti-rabbit immunoglobulin G (IgG) horseradish peroxidase (HRP) (W401B, 1:10,000, Promega) or anti-mouse IgG HRP (W402B, 1:10,000, Promega) conjugate for 1 hour. The secondary antibody was washed three times with washing buffer and then evenly coated with enhanced chemiluminescence (ECL) Western blotting detection reagents (GE Healthcare) for 30 s. The membrane was immediately exposed to Fuji Medical X-ray film (Fujifilm) at room temperature for various periods in a film cassette. Protein levels were standardized with the signal from the β -actin probe.

In vivo antitumor activity studies. BALB/c-nu/nu mice (female, $n = 4$) were inoculated subcutaneously with HT29 or HT29/ox cells (1×10^7 /ml). Tumors were allowed to grow for 1 week (tumor size at this point was about 40 mm³). Mice were then treated intravenously three times at 2-day intervals with oxaliplatin (8 mg/kg) or DACHPt/m (4 mg/kg) on a platinum base. Antitumor activity was evaluated in terms of tumor size (V) with the following equation:

$$V = a \times b^2 / 2$$

Here, a and b are the major and minor axes, respectively, of the tumor as measured by a caliper.

Intravital observation of the in vivo behavior of F-DACHPt/m. Intravital observation of F-DACHPt/m was performed as described (49). Female BALB/c mice (6 to 8 weeks old) were inoculated subcutaneously with HT29 cells (1×10^7 /ml). After 5 days, when the tumor volumes reached 70 mm³, F-DACHPt/m (10 mg/kg) was administered intravenously. At 2, 4, 12, and 24 hours after treatment, mice were anesthetized with 2.5% isoflurane (Abbott Japan) with a Univentor 400 Anesthesia Unit (Univentor). An arc-shaped incision was made around the subcutaneous tumor, and the skin flap was elevated without injuring the feeding vessels. The mouse was placed directly onto a thermoplate (Tokai Hit), and the skin flap was everted and stretched with several bent 30-gauge needles. The plasma membrane stain, CellMask Deep Red, was directly applied to the subcutaneous tumor, and a coverslip (Muto Pure Chemicals) was attached with just enough pressure to flatten the tumor surface. All in vivo images were acquired with a Nikon A1R CLSM attached to an upright Eclipse FN1 (Nikon). The A1R incorporates a conventional galvano scanner and a high-speed resonant scanner. The latter allows an acquisition speed of 30 frames per second while maintaining a relatively high resolution of 512 \times 512 scanned points. BODIPY FL, BODIPY TR, and CellMask were excited with three lasers (488-nm Ar, 560-nm He-Ne, and 640-nm He-Ne lasers), and the fluorescent signals were detected. Laser powers were kept at 19.5 mW for 488-nm Ar, 7.5 mW for 561-nm He-Ne, and 1 mW for 640-nm He-Ne.

Statistical analysis. Data are presented as means \pm SEM. The significant differences between the groups were analyzed by a Student's t test, and a P value of <0.05 was considered significant.

SUPPLEMENTARY MATERIAL

www.sciencetranslationalmedicine.org/cgi/content/full/3/64/64ra2/DC1

Fig. S1. Synthetic scheme of BODIPY FL-PEG-b-P(Glu)-BODIPY TR.

Fig. S2. Size distribution of DACHPt/m and F-DACHPt/m as determined by dynamic light scattering.

Fig. S3. Fluorescent images of HT29 cells after 6-hour incubation with F-DACHPt/m at 37°C and 4°C.

Fig. S4. In vitro CLSM observation of dissociation of F-DACHPt/m in the late endosomes/lysosomes.

Fig. S5. In vitro cytotoxicity of oxaliplatin and DACHPt/m against a human cancer cell panel.

Fig. S6. Knockdown of MT1Q and MTR restores the sensitivity of HT29/ox to oxaliplatin.

Fig. S7. Schematic illustration of experimental settings of in vivo CLSM.

Table S1. Coefficient of correlation between the GI_{50} s of free oxaliplatin or DACHPt/m and the expression levels of genes involved in the sensitivity or resistance of cells to platinum compounds.

Video S1. In vitro live imaging.

Video S2. In vivo live imaging (immediately after injection).

Video S3. In vivo live imaging (12 hours after injection).

REFERENCES AND NOTES

1. A. Jemal, R. Siegel, E. Ward, Y. Hao, J. Xu, M. J. Thun, Cancer statistics, 2009. *CA Cancer J. Clin.* **59**, 225–249 (2009).
2. T. M. Allen, P. R. Cullis, Drug delivery systems: Entering the mainstream. *Science* **303**, 1818–1822 (2004).
3. M. Ferrari, Cancer nanotechnology: Opportunities and challenges. *Nat. Rev. Cancer* **5**, 161–171 (2005).
4. V. P. Torchilin, Recent advances with liposomes as pharmaceutical carriers. *Nat. Rev. Drug Discov.* **4**, 145–160 (2005).
5. R. Duncan, The dawning era of polymer therapeutics. *Nat. Rev. Drug Discov.* **2**, 347–360 (2003).
6. Y. Matsumura, H. Maeda, A new concept for macromolecular therapeutics in cancer chemotherapy: Mechanism of tumorotropic accumulation of proteins and the antitumor agent Smancs. *Cancer Res.* **46**, 6387–6392 (1986).
7. M. E. Davis, Z. G. Chen, D. M. Shin, Nanoparticle therapeutics: An emerging treatment modality for cancer. *Nat. Rev. Drug Discov.* **7**, 771–782 (2008).
8. N. Nishiyama, K. Kataoka, Current state, achievements, and future prospects of polymeric micelles as nanocarriers for drug and gene delivery. *Pharmacol. Ther.* **112**, 630–648 (2006).
9. M. Yokoyama, M. Miyauchi, N. Yamada, T. Okano, Y. Sakurai, K. Kataoka, S. Inoue, Characterization and anticancer activity of the micelle-forming polymeric anticancer drug adriamycin-conjugated poly(ethylene glycol)-poly(aspartic acid) block copolymer. *Cancer Res.* **50**, 1693–1700 (1990).
10. K. Kataoka, G. S. Kwon, M. Yokoyama, T. Okano, Y. Sakurai, Block copolymer micelles as vehicles for drug delivery. *J. Control. Release* **24**, 119–132 (1993).
11. K. Kataoka, A. Harada, Y. Nagasaki, Block copolymer micelles for drug delivery: Design, characterization and biological significance. *Adv. Drug Deliv. Rev.* **47**, 113–131 (2001).
12. A. V. Kabanov, E. V. Batrakova, D. W. Miller, Pluronic block copolymers as modulators of drug efflux transporter activity in the blood–brain barrier. *Adv. Drug Deliv. Rev.* **55**, 151–164 (2003).
13. Y. Matsumura, K. Kataoka, Preclinical and clinical studies of anticancer agent-incorporating polymeric micelles. *Cancer Sci.* **100**, 572–579 (2009).
14. Y. Matsumura, T. Hamaguchi, T. Ura, K. Muro, Y. Yamada, Y. Shimada, K. Shiro, T. Okusaka, H. Ueno, M. Ikeda, N. Watanabe, Phase I clinical trial and pharmacokinetic evaluation of NK911, a micelle-encapsulated doxorubicin. *Br. J. Cancer* **91**, 1775–1781 (2004).
15. T. Hamaguchi, K. Kato, H. Yasui, C. Morizane, M. Ikeda, H. Ueno, K. Muro, Y. Yamada, T. Okusaka, K. Shiro, Y. Shimada, H. Nakahama, Y. Matsumura, A phase I and pharmacokinetic study of NK105, a paclitaxel-incorporating micellar nanoparticle formulation. *Br. J. Cancer* **97**, 170–176 (2007).
16. T. Hamaguchi, T. Doi, T. Eguchi-Nakajima, K. Kato, Y. Yamada, Y. Shimada, N. Fuse, A. Ohtsu, S. Matsumoto, M. Takahashi, Y. Matsumura, Phase I study of NK012, a novel SN-38-incorporating micellar nanoparticle, in adult patients with solid tumors. *Clin. Cancer Res.* **16**, 5058–5066 (2010).
17. R. H. Wilson, R. Plummer, J. Adam, M. M. Eatock, A. V. Boddy, M. Griffin, R. Miller, Y. Matsumura, T. Shimizu, H. Calvert, Phase I and pharmacokinetic study of NC-6004, a new platinum entity of cisplatin-conjugated polymer forming micelles. *J. Clin. Oncol.* **26**, 2573 (2008).
18. R. Dent, M. Trudeau, K. I. Pritchard, W. M. Hanna, H. K. Kahn, C. A. Sawka, L. A. Lickley, E. Rawlinson, P. Sun, S. A. Narod, Triple-negative breast cancer: Clinical features and patterns of recurrence. *Clin. Cancer Res.* **13**, 4429–4434 (2007).
19. J. A. Hubbell, Materials science. Enhancing drug function. *Science* **300**, 595–596 (2003).
20. T. Minko, P. Kopecková, J. Kopeček, Efficacy of the chemotherapeutic action of HPMA copolymer-bound doxorubicin in a solid tumor model of ovarian carcinoma. *Int. J. Cancer* **86**, 108–117 (2000).
21. D. Kim, E. S. Lee, K. T. Oh, Z. G. Gao, Y. H. Bae, Doxorubicin-loaded polymeric micelle overcomes multidrug resistance of cancer by double-targeting folate receptor and early endosomal pH. *Small* **4**, 2043–2050 (2008).
22. K. Cho, X. Wang, S. Nie, Z. G. Chen, D. M. Shin, Therapeutic nanoparticles for drug delivery in cancer. *Clin. Cancer Res.* **14**, 1310–1316 (2008).
23. H. Cabral, N. Nishiyama, S. Okazaki, H. Koyama, K. Kataoka, Preparation and biological properties of dichloro(1,2-diaminocyclohexane)platinum(II) (DACHPt)-loaded polymeric micelles. *J. Control. Release* **101**, 223–232 (2005).
24. H. Cabral, N. Nishiyama, K. Kataoka, Optimization of (1,2-diamino-cyclohexane)platinum(II)-loaded polymeric micelles directed to improved tumor targeting and enhanced antitumor activity. *J. Control. Release* **121**, 146–155 (2007).
25. N. D. Sonawane, J. R. Thiagarajah, A. S. Verkman, Chloride concentration in endosomes measured using a ratioable fluorescent Cl^- indicator: Evidence for chloride accumulation during acidification. *J. Biol. Chem.* **277**, 5506–5513 (2002).
26. N. Nishiyama, F. Koizumi, S. Okazaki, Y. Matsumura, K. Nishio, K. Kataoka, Differential gene expression profile between PC-14 cells treated with free cisplatin and cisplatin-incorporated polymeric micelles. *Bioconjug. Chem.* **14**, 449–457 (2003).
27. I. D. Johnson, H. C. Kang, R. P. Haugland, Fluorescent membrane probes incorporating dipyrrometheneboron difluoride fluorophores. *Anal. Biochem.* **198**, 228–237 (1991).
28. S. Arnould, I. Hennebel, P. Canal, R. Bugat, S. Guichard, Cellular determinants of oxaliplatin sensitivity in colon cancer cell lines. *Eur. J. Cancer* **39**, 112–119 (2003).
29. L. Kelland, The resurgence of platinum-based cancer chemotherapy. *Nat. Rev. Cancer* **7**, 573–584 (2007).
30. E. Raymond, S. Faivre, S. Chaney, J. Woynarowski, E. Cvitkovic, Cellular and molecular pharmacology of oxaliplatin. *Mol. Cancer Ther.* **1**, 227–235 (2002).
31. F. R. Luo, T. Y. Yen, S. D. Wyrick, S. G. Chaney, High-performance liquid chromatographic separation of the biotransformation products of oxaliplatin. *J. Chromatogr. B Biomed. Sci. Appl.* **724**, 345–356 (1999).
32. F. R. Luo, S. D. Wyrick, S. G. Chaney, Biotransformations of oxaliplatin in rat blood in vitro. *J. Biochem. Mol. Toxicol.* **13**, 159–169 (1999).
33. R. Duncan, Polymer conjugates as anticancer nanomedicines. *Nat. Rev. Cancer* **6**, 688–701 (2006).
34. T. Yamori, A. Matsunaga, S. Sato, K. Yamazaki, A. Komi, K. Ishizu, I. Mita, H. Edatsugi, Y. Matsuba, K. Takezawa, O. Nakanishi, H. Kohno, Y. Nakajima, H. Komatsu, T. Andoh, T. Tsuruo, Potent antitumor activity of MS-247, a novel DNA minor groove binder, evaluated by an *in vitro* and *in vivo* human cancer cell line panel. *Cancer Res.* **59**, 4042–4049 (1999).
35. S. Yaguchi, Y. Fukui, I. Koshimizu, H. Yoshimi, T. Matsuno, H. Gouda, S. Hirono, K. Yamazaki, T. Yamori, Antitumor activity of ZSTK474, a new phosphatidylinositol 3-kinase inhibitor. *J. Natl. Cancer Inst.* **98**, 545–556 (2006).
36. A. Vekris, D. Meynard, M. C. Haaz, M. Bayssas, J. Bonnet, J. Robert, Molecular determinants of the cytotoxicity of platinum compounds: The contribution of *in silico* research. *Cancer Res.* **64**, 356–362 (2004).
37. S. L. Kelley, A. Basu, B. A. Teicher, M. P. Hacker, D. H. Hamer, J. S. Lazo, Overexpression of metallothionein confers resistance to anticancer drugs. *Science* **241**, 1813–1815 (1988).
38. J. Holford, P. J. Beale, F. E. Boxall, S. Y. Sharp, L. R. Kelland, Mechanisms of drug resistance to the platinum complex ZD0473 in ovarian cancer cell lines. *Eur. J. Cancer* **36**, 1984–1990 (2000).
39. P. M. Deegan, I. S. Pratt, M. P. Ryan, The nephrotoxicity, cytotoxicity and renal handling of a cisplatin-methionine complex in male Wistar rats. *Toxicology* **89**, 1–14 (1994).
40. R. M. Goldberg, D. J. Sargent, R. F. Morton, C. S. Fuchs, R. K. Ramanathan, S. K. Williamson, B. P. Findlay, H. C. Pitot, S. R. Alberts, A randomized controlled trial of fluorouracil plus leucovorin, irinotecan, and oxaliplatin combinations in patients with previously untreated metastatic colorectal cancer. *J. Clin. Oncol.* **22**, 23–30 (2004).
41. D. Wang, S. J. Lippard, Cellular processing of platinum anticancer drugs. *Nat. Rev. Drug Discov.* **4**, 307–320 (2005).
42. I. Pastan, M. M. Gottesman, K. Ueda, E. Lovelace, A. V. Rutherford, M. C. Willingham, A retrovirus carrying an *MDR1* cDNA confers multidrug resistance and polarized expression of P-glycoprotein in MDCK cells. *Proc. Natl. Acad. Sci. U.S.A.* **85**, 4486–4490 (1988).
43. R. K. Jain, Delivery of molecular and cellular medicine to solid tumors. *Adv. Drug Deliv. Rev.* **46**, 149–168 (2001).
44. Y. Saito, M. Yasunaga, J. Kuroda, Y. Koga, Y. Matsumura, Antitumor activity of NK012, SN-38-incorporating polymeric micelles, in hypovascular orthotopic pancreatic tumour. *Eur. J. Cancer* **46**, 650–658 (2010).
45. M. Mishima, G. Samimi, A. Kondo, X. Lin, S. B. Howell, The cellular pharmacology of oxaliplatin resistance. *Eur. J. Cancer* **38**, 1405–1412 (2002).

46. Y. Akiyama, Y. Nagasaki, K. Kataoka, Synthesis of heterotelechelic poly(ethylene glycol) derivatives having α -benzaldehyde and ω -pyridyl disulfide groups by ring opening polymerization of ethylene oxide using 4-(diethoxymethyl)benzyl alkoxide as a novel initiator. *Bioconjug. Chem.* **15**, 424–427 (2004).
47. N. Nishiyama, S. Okazaki, H. Cabral, M. Miyamoto, Y. Kato, Y. Sugiyama, K. Nishio, Y. Matsumura, K. Kataoka, Novel cisplatin-incorporated polymeric micelles can eradicate solid tumors in mice. *Cancer Res.* **63**, 8977–8983 (2003).
48. W. H. Daly, D. Poche, The preparation of N-carboxyanhydrides of α -amino acids using bis(trichloromethyl)carbonate. *Tetrahedron Lett.* **29**, 5859–5862 (1988).
49. Y. Matsumoto, T. Nomoto, H. Cabral, Y. Matsumoto, S. Watanabe, R. J. Christie, K. Miyata, M. Oba, T. Ogura, Y. Yamasaki, N. Nishiyama, T. Yamasoba, K. Kataoka, Direct and instantaneous observation of intravenously injected substances using intravital confocal micro-videography. *Biomed. Opt. Express* **1**, 1209–1216 (2010).
50. **Acknowledgments:** M.M. thanks J. Ghaugas for his support and suggestions for preparing the manuscript and S. Hiro for his help with in silico data analysis. **Funding:** This research was supported in part by Funding Program for World-Leading Innovative R&D on Science and Technology (FIRST Program) from the Japan Society for the Promotion of Science

(JSPS) and the Core Research Program for Evolutional Science and Technology (CREST) from the Japan Science and Technology Agency (JST). **Author contributions:** M.M. and H.C. designed and performed the experiments, analyzed the results, and wrote the manuscript. Y.M. performed the imaging experiments. S.W. performed the siRNA knockdown studies. T.Y. conducted human cell panel analysis. M.R.K. edited the manuscript. N.N. supervised the project and wrote the manuscript. K.K. supervised the project and edited the manuscript. **Competing interests:** The authors declare that they have no competing interests.

Submitted 14 June 2010

Accepted 10 December 2010

Published 5 January 2011

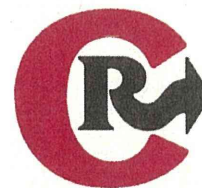
10.1126/scitranslmed.3001385

Citation: M. Murakami, H. Cabral, Y. Matsumoto, S. Wu, M. R. Kano, T. Yamori, N. Nishiyama, K. Kataoka, Improving drug potency and efficacy by nanocarrier-mediated subcellular targeting. *Sci. Transl. Med.* **3**, 64ra2 (2011).



Contents lists available at ScienceDirect

Journal of Controlled Release

journal homepage: www.elsevier.com/locate/jconrel

Enhanced magnetic resonance imaging of experimental pancreatic tumor *in vivo* by block copolymer-coated magnetite nanoparticles with TGF- β inhibitor

Michiaki Kumagai^{a,e,1}, Mitsunobu R. Kano^{b,f,1}, Yasuyuki Morishita^b, Motomi Ota^a, Yutaka Imai^a, Nobuhiro Nishiyama^{a,e,f}, Masaki Sekino^c, Shoogo Ueno^d, Kohei Miyazono^{b,f}, Kazunori Kataoka^{a,e,f,*}

^a Department of Materials Engineering, Graduate School of Engineering, The University of Tokyo, 7-3-1 Hongo, Bunkyo-ku, Tokyo 113-8656, Japan

^b Department of Molecular Pathology, Graduate School of Medicine, The University of Tokyo, 7-3-1 Hongo, Bunkyo-ku Tokyo 113-0033, Japan

^c Department of Advanced Energy, Graduate School of Frontier Sciences, The University of Tokyo, 5-1-5, Kashiwanoha, Kashiwa-shi, Chiba, 277-8561, Japan

^d Department of Applied Quantum Physics, Graduate School of Engineering, Kyushu University, 6-10-1 Hakozaki, Higashi-ku Fukuoka 812-8581, Japan

^e Center for Disease Biology and Integrative Medicine, School of Medicine, The University of Tokyo, 7-3-1 Hongo, Bunkyo-ku, Tokyo 113-0033, Japan

^f Center for NanoBio Integration, The University of Tokyo, 7-3-1 Hongo, Bunkyo-ku, Tokyo 113-8656, Japan

ARTICLE INFO

Article history:

Received 13 March 2009

Accepted 5 June 2009

Available online 12 June 2009

Keyword:

Magnetic resonance imaging

Pancreatic cancer

TGF- β

Magnetite nanoparticles

Poly(ethylene glycol)

ABSTRACT

Early detection of solid tumors, particularly pancreatic cancer, is of substantial importance in clinics. Enhanced magnetic resonance imaging (MRI) with iron oxide nanoparticles is an available way to detect the cancer. The effective and selective accumulation of these nanoparticles in the tumor tissue is needed for improved imaging, and in this regard, their longevity in the blood circulation time is crucial. We developed here block copolymer-coated magnetite nanoparticles for pancreatic cancer imaging, by means of a chelation between the carboxylic acid groups in poly(ethylene glycol)–poly(aspartic acid) block copolymer (PEG–PAsp) and Fe on the surface of the iron oxide nanoparticles. These nanoparticles had considerably narrow distribution, even upon increased ionic strength or in the presence of fetal bovine serum. The PEG–PAsp-coated nanoparticles were further shown to be potent as a contrast agent for enhanced MRI for an experimental pancreatic cancer, xenografts of the human-derived BxPC3 cell line in BALB/c nude mice, with combined administration of TGF- β inhibitor. Iron staining of tumor tissue confirmed the accumulation of the nanoparticles in tumor tissue. Use of the PEG–PAsp-coated magnetite nanoparticles, combined with the TGF- β inhibitor, is of promising clinical importance for the detection of intractable solid cancers, including pancreatic cancer.

© 2009 Elsevier B.V. All rights reserved.

1. Introduction

Pancreatic cancer, one of the intractable solid tumors, is the fourth leading cause of cancer-related deaths in the United States and the fifth in Japan [1]. The average survival period of patients suffering from advanced pancreatic adenocarcinoma is still extremely short, only 6 months, despite recent progress in the chemotherapies [2]. Although cancer detection and treatment have been greatly improved through the development of diagnostic imaging modalities, it is still difficult to detect pancreatic cancer [3]. Consequently, the development of diagnostic systems to detect these cancers is of great importance.

Recently, superparamagnetic iron oxide (SPIO) nanoparticles composed of either magnetite (Fe_3O_4) or maghemite ($\text{g-Fe}_2\text{O}_3$) have been studied as contrast agents for magnetic resonance (MR) imaging [4]. Commercial application for human diagnosis based on SPIO

particles is currently available. However, since cancer detection requires the systemic administration of iron oxide nanoparticles, the circulation time of the particles must be prolonged. Several studies have already reported that the behavior of magnetic nanoparticles in the bloodstream depends closely on their nanoscale morphology, including overall diameter, size distribution, or nature of the surface [5,6]. Additionally, the surface modification of iron oxide nanoparticles has proved a versatile strategy for improving their biological performance, including the reduction of immunogenicity and enhancement of targeted delivery to specific tissues [7]. However, the overall correlation between the surface modification of nanoparticles and their *in vivo* behavior remains to be further elucidated.

Various methods of stabilization of SPIO nanoparticles have been reported to date [8]. One of the most feasible approaches could be the stabilization of SPIO by coated with biocompatible polymers [9]. Suitable polymers, including poly(ethylene glycol) (PEG) and its block copolymers, are promising for the development of SPIO systems with defined surface properties. This coating of particles with PEG, or PEGylation, to avoid their uptake by the reticuloendothelial system, is under intensive investigation. We also previously reported the accumulation of β -FeOOH nanoparticles coated with PEG–poly(α,β -aspartic acid) block copolymer

* Corresponding author. Department of Materials Engineering, Graduate School of Engineering, The University of Tokyo, 7-3-1 Hongo, Bunkyo-ku, Tokyo 113-8656, Japan.
E-mail address: kataoka@bmyw.t.u-tokyo.ac.jp (K. Kataoka).

¹ Equal contribution.

(PEG–PAsp) into experimental colon adenocarcinoma, which could be applicable for tumor-selective MR imaging [10]. The multivalent bonding of PEG-based block copolymer to magnetic nanoparticles may thus help to facilitate the accumulation of these nanoparticles into some solid tumors. However, magnetic nanoparticles of any design have not yet been successful in exhibiting sufficient accumulation in intractable solid cancers, including pancreatic adenocarcinoma [1]. In addition to improving the performance of iron-based contrast agents (e.g. biocompatibility), the co-administration of adjuvant small molecules could increase the accumulation of these agents in target cancer tissue. In fact, we have recently shown that the administration of the small molecule TGF- β inhibitor (LY364947) at a low dose [11], which could minimize the potential side effects of the TGF- β inhibitor, can alter the tumor microenvironment and enhance the EPR effect in these cancers [12]. Therefore, the combined use of TGF- β inhibitor could be promising to diagnose intractable cancers with a long-circulating MRI contrast agent. Here, we demonstrated the successful MR imaging of experimental pancreatic cancer by the systemic administration of newly developed SPIO nanoparticles coated by PEG–PAsp in aid of TGF- β inhibitor.

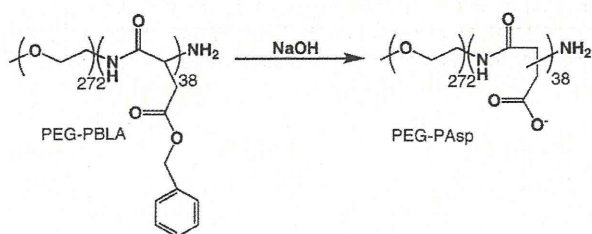
2. Materials and methods

2.1. Reagents

β -benzyl L-aspartate and bis(trichloromethyl)carbonate (triphosgene) were purchased from Sigma-Aldrich Corporation (St. Louis, MO, USA) and Tokyo Chemical Industry Co., Ltd. (Tokyo, Japan), respectively. α -Methoxy- ω -amino-poly(ethylene glycol) ($\text{CH}_3\text{O-PEG-NH}_2$; $M_w = 12000$) was purchased from NOF Corporation (Tokyo, Japan). Tetrahydrofuran (THF), *n*-hexane, *N,N*-dimethylformamide (DMF), CH_2Cl_2 were doubly-distilled according to the standard procedures. The magnetite nanoparticles were supplied by Toda Kogyo Corporation (Hiroshima, Japan; average particle size of magnetite: 10 nm). Resovist® was obtained from Bayer HealthCare Co., Ltd. (Osaka, Japan). TGF- β inhibitor was purchased from EMD Chemicals Inc. (San Diego, CA, USA) (LY364947; catalog no. 616451).

2.2. Synthesis of poly(ethylene glycol)-poly(α,β -aspartic acid) block copolymer (PEG–PAsp)

PEG–PAsp was synthesized by a previously reported procedure [13]. Briefly, poly(ethylene glycol)-*b*-poly(β -benzyl L-aspartate) block copolymer (PEG–PBLA) was prepared by ring-opening polymerization of *N*-carboxy anhydride of β -benzyl L-aspartate (BLA-NCA) from the ω -NH $_2$ group of PEG ($M_w = 1.2 \times 10^4$). Molecular weight distribution of PEG–PBLA was narrow as $M_w/M_n = 1.06$, which was determined by gel permeation chromatography [columns: TSK-gel G3000HHR, G4000HHR (Tosoh, Yamaguchi, Japan); eluent: DMF containing 10 mM LiCl; flow rate: 0.8 ml/min; detector: refractive index (RI); temperature: 40 °C]. The composition of these block copolymers was determined by ^1H NMR from peak intensity ratios of methylene protons of PEG (OCH_2CH_2 ; $d = 3.7$ ppm) and phenyl protons of the β -benzyl groups of PBLA ($-\text{CH}_2\text{C}_6\text{H}_5$; $d = 7.3$ ppm). The polymerization degree of BLA in block copolymer was calculated to be 38. The benzyl groups of PEG–PBLA were then removed by alkaline hydrolysis using 0.1 N NaOH to obtain PEG–PAsp as follows:



2.3. Preparation of PEG–PAsp-coated magnetite nanoparticles

PEG–PAsp-coated magnetite nanoparticles were prepared according to the previous method with slight modification [10]. Briefly, magnetite solution was quickly added to an aqueous solution of PEG–PAsp with varying feed molar ratios of aspartic acid residues to Fe ($[\text{Asp}]/[\text{Fe}]$) in the range of 0.01 to 1. The final concentration of magnetite was adjusted to 10 mmol/l. The mixed solutions were incubated at room temperature for 24 h to obtain magnetite nanoparticles coated with PEG–PAsp. Purification of the PEG–PAsp-coated magnetite nanoparticles was carried out by ultrafiltration (MWCO 200 000; polysulfone membrane, Toyo Roshi Co. Ltd., Tokyo, Japan).

2.4. Physicochemical characterization of the nanoparticles

The morphology and size distribution of the nanoparticles were examined by transmission electron microscopy (H-7000, Hitachi, Ltd., Tokyo, Japan) at an accelerating voltage of 75 kV. The TEM samples were prepared by mounting a drop of aqueous iron oxide nanoparticles suspension on carbon-coated 400 mesh Cu grids and allowing them to dry in air. Fourier transform infrared (FT-IR) spectra were obtained using a FT-IR spectrophotometer (FT/IR615, JASCO Corporation, Hachioji, Tokyo, Japan) with a resolution of 4 cm^{-1} . To characterize the interaction between block copolymer and magnetite nanoparticles, a small amount of nanoparticles powder was milled with KBr, and then pressed into a disc for analysis. Each spectrum was scanned 64 times to increase the signal-to-noise ratio. The Fe content in the nanoparticles was determined by ion coupled plasma-mass spectroscopy (ICP-MS, 4500, Hewlett Packard, Palo Alto, CA, USA). The amount of adsorbed block copolymer on magnetite nanoparticles was measured by thermogravimetric analysis (TGA) (EXSTAR6200 TG/DTA, Seiko Instruments Inc., Chiba, Japan) in nitrogen atmosphere with a heating rate of 10 °C/min in the temperature range of 25–1100 °C.

2.5. Light scattering and ζ -potential measurements

The size distribution of the PEG–PAsp-coated magnetite nanoparticles was examined by dynamic light scattering (DLS) DLS-7000 (Otsuka Electronics Co., Ltd., Osaka, Japan). Vertically polarized light with a wavelength of 488 nm from an Ar-ion laser (15 mW) was used as the incident beam. All measurements were conducted at 37 °C, and the data were analyzed by the cumulant method to determine the hydrodynamic diameters of the particles. The ζ -potential of PEG–PAsp-coated magnetite nanoparticles at 37 °C was measured by a Zetasizer NanoZS instrument equipped with a DTS5001 cell (Malvern Instruments Ltd., Worcestershire, UK).

2.6. Characterization of the r_2 relaxivities

The MR contrast effect of the magnetite nanoparticles was examined by measuring their proton relaxivities, r_2 , of which the definition is the slope of the concentration dependence given as:

$$1/T_2 = 1/T_2(0) + r_2[\text{Fe}]$$

Thus, a plot of $1/T_2$ versus concentration gives the relaxivity as the slope, where T_2 is the transversal relaxation time, $1/T_2$ is the transversal relaxation rate constant in the presence of a paramagnetic species, and $1/T_2(0)$ is the transversal relaxation rate constant in the absence of a paramagnetic species. The magnetite nanoparticles were dispersed into deionized water at concentrations of 0.5, 1.0, 1.5, 2.0, and 2.5 mM and the T_2 of these nanoparticle solutions was measured at 25 °C in water with a 0.47 T minispectrometer (Minispec, Bruker

Optics Inc., Woodlands, TX, USA) using the Carr–Purcell–Meiboom–Gill (CPMG) method [14].

2.7. *In vivo* MR imaging

The BxPC3 human pancreatic adenocarcinoma cell line was obtained from the American Type Culture Collection (Manassas, VA, USA). The BxPC3 cells were grown in RPMI 1640 medium supplemented with 10% FBS. BALB/c nude mice (female, 5–6 weeks of age), obtained from Charles River Laboratories Japan Inc. (Tokyo, Japan), were inoculated subcutaneously with BxPC3 cells (1×10^7 cells/mouse). After 3–4 weeks, MR imaging of the tumors was conducted with a 4.7 T scanner (INOVA200, Varian, Inc., Palo Alto, CA, USA). Twenty-four hours prior to the *in vivo* MR imaging, animals were treated with TGF- β inhibitor, 5 mg/ml in 4 μ l of DMSO and diluted by 100 μ l of PBS, at 1 mg/kg by intraperitoneal injection. Subsequently, the mice were injected at a dose of 0.1 mmolFe/kg, with Resovist[®] or PEG–PAsp-coated magnetite nanoparticles. A total of 4 conditions ($n = 5$ mice each) were investigated, i.e. with or without TGF- β inhibitor for both Resovist[®] or PEG–PAsp-coated magnetite nanoparticles. Imaging was performed at different temporal points (e.g., preinjection, 1 h postinjection, and 2 h postinjection). For the T_2 -weighted MR imaging of live mice, the following parameters were adopted: spin-echo method, point resolution = $234 \times 234 \mu\text{m}$, section thickness = 2.0 mm, TE = 60 ms, TR = 3000 ms, number of acquisitions = 5. All animals were treated in accordance with the guidelines of the Animal Ethics Committee of the University of Tokyo.

2.8. Histology

The excised samples were fixed overnight in 4% paraformaldehyde and then paraffin-embedded. Embedded samples were thin sliced at 10 μm thick and then stained using an Iron Stain Kit (Muto Pure Chemicals Co., Ltd., Tokyo, Japan), based on McFadzean's protocol [15], with nuclear post-staining by 1% Safranin O. Iron staining was observed using an AX80 microscope (Olympus Corporation, Tokyo, Japan). The photographs were further quantified using Adobe Photoshop software (Adobe Systems Incorporated, San Jose, CA, USA), ImageJ software (National Institute of Health, MD, USA), and Microsoft Excel software (Microsoft Corporation, Redmond, WA, USA).

3. Results and discussion

3.1. The physicochemical properties of the PEG–PAsp-coated magnetite nanoparticle: diameter and surface polymer density

For solid tumor diagnosis, it is important to develop well-designed magnetite nanoparticles. The key physicochemical properties of

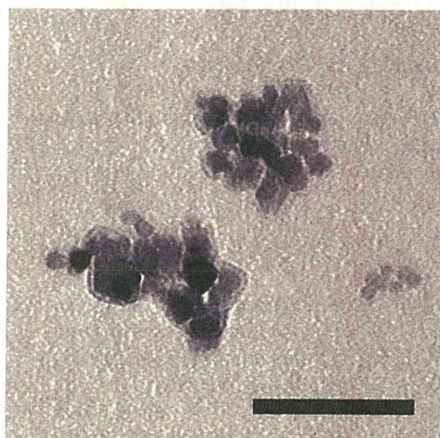


Fig. 1. TEM image of the PEG–PAsp-coated magnetite nanoparticles. Bar: 100 nm.

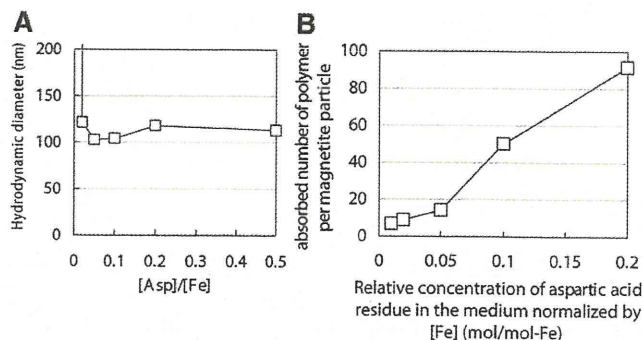


Fig. 2. Physicochemical properties of the PEG–PAsp-coated magnetite nanoparticles. (A) Hydrodynamic diameter vs. relative concentration of aspartic acid residue in the medium normalized by [Fe] (mol/mol-Fe) ($= [\text{Asp}]/[\text{Fe}]$), and (B) Change in the adsorbed density of PEG–PAsp on the magnetite surface estimated from TGA analysis with a bulk concentration of PEG–PAsp. Temperature = 37 $^{\circ}\text{C}$; medium: distilled water.

magnetite nanoparticles are size, surface polymer density, and surface charge, since these characteristics can affect accumulation of magnetite nanoparticles to solid tumor. The PEG–PAsp-coated magnetite nanoparticles were prepared by mixing solutions of magnetite nanoparticles and PEG–PAsp with various molar ratios of the Asp residues to Fe (Asp/Fe); Asp/Fe ranged from 0.01 to 0.5, where $[\text{Fe}] = 10 \text{ mmol/l}$. As seen in Fig. 1, the transmission electron microscopy (TEM) image with 75 kV accelerating voltage of nanoparticles mounted on carbon grid from aqueous solution revealed that PEG–PAsp-coated magnetite nanoparticles take a cubic shape with a mean particle diameter of approximately 10 nm. The PEG–PAsp coating was observed as a layer with a thickness of approximately 5 nm, surrounding the magnetite nanoparticles. It was also observed in the TEM image that these PEG–PAsp-coated nanoparticles form clusters with a size range of 100 nm.

The hydrodynamic diameter of these nanoparticles in aqueous medium was then measured with DLS and shown to be in the range of 100 to 120 nm with unimodal distribution, for Asp/Fe ratios ranging from 0.02–0.5. This DLS data is consistent with the cluster formation of nanoparticles indicated from TEM images. However, with a lowered Asp/Fe ratio as 0.01, the hydrodynamic diameter increased significantly (Fig. 2A). This result indicates that there is a critical surface concentration of PEG to effectively prevent the PEG–PAsp-coated magnetite nanoparticles from the agglomeration. The purified nanoparticles were stable in distilled water as 100 nm-scaled cluster at room temperature as well as at 37 $^{\circ}\text{C}$, maintaining the initial photon count and distribution in DLS analysis for at least one month, even after the ultrafiltration to remove free PEG–PAsp possibly remained in the reactant.

The density of the PEG–PAsp block copolymer on the magnetite particle surface was estimated by TGA. Here, nanoparticles were heated in the nitrogen atmosphere to selectively vaporize the polymer fraction. Eventually, the amount of absorbed polymer on the surface of the nanoparticles was measured from the weight change by heating. The polymer density was then calculated from the TGA measurement for all the nanoparticles, assuming the cubic morphology as evidenced by microscopy and a density of 5.05 g/cm^3 for magnetite. As seen in Fig. 2B, the number of polymer strands on the nanoparticle surface was as high as 100. This data suggests that the PEG density on the magnetite nanoparticles is a little lower than that of PEGylated gold nanoparticles prepared through the surface tethering of PEG-SH [16].

3.2. The mechanism of PEG–PAsp adsorption on the magnetite nanoparticles

To confirm the formation of PEG–PAsp coating on the magnetite nanoparticles, the ζ -potential of bare and PEG–PAsp-coated magnetite nanoparticles was measured in 10 mM MOPS buffer as a function of

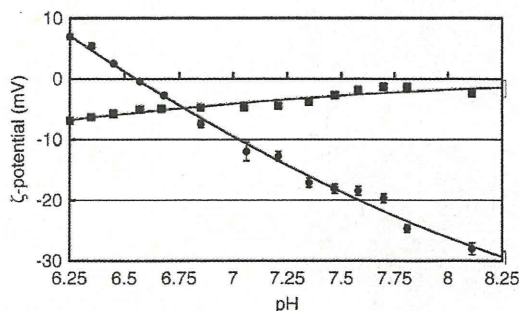


Fig. 3. Change in the ζ -potential with pH for bare (●) and PEG-PAsp-coated (■) magnetite nanoparticles. Temperature = 37 °C; medium: 10 mM MOPS buffer.

pH (Fig. 3). The isoelectric point (IEP) of the bare magnetite nanoparticles was estimated as approximately 6.6, which is consistent with the reported IEP value of iron oxide [17]. In a lower pH (below the IEP), the magnetite nanoparticle surface was protonated to result in a positive ζ -potential. Thus, in this pH range, electrostatic attraction between positively-charged magnetite nanoparticles and negatively charged PEG-PAsp is expected to occur, allowing the PEG-PAsp adsorption to the nanoparticle surface. Alternatively, the bare magnetite nanoparticles possess negative ζ -potential at physiological pH 7.4, whereas the ζ -potential shifted to the neutral value for PEG-PAsp modified nanoparticles in 10 mM MOPS buffer (pH 7.4), being consistent with the formation of a PEG shell layer. Also, these data suggest that there should be an adsorption mechanism other than simple electrostatic interaction, because magnetite has a negative ζ -potential value at pH 7.4 to induce electrostatic repulsive force against negatively charged carboxylates in PEG-PAsp. The adsorption mechanism under physiological pH was suggested to be the monodentate chelation (I) (Fig. 4) from the result of Fourier transform infrared spectroscopy [18], as explained in detail in Supplemental Text with Supplemental Fig. 1 and Supplemental Table 1.

3.3. Comparison study of the physicochemical characteristics of the PEG-PAsp- and dextran-coated magnetite nanoparticles

The MRI detection limit was compared between the PEG-PAsp- and dextran-coated magnetite nanoparticles in the field of 0.47 T at 25 °C from the relaxivity r_2 , exhibiting the sensitivity of the T_2 MRI contrast agent. The dextran-coated magnetite used in this study was the one already in clinical use, Resovist®. Eventually, the relaxivity r_2 of the PEG-PAsp nanoparticle was calculated to be $138 \text{ mM}^{-1} \text{ s}^{-1}$, the value similar to Resovist® [19].

The hydrodynamic diameter observed between the PEG-PAsp-coated and dextran-coated magnetite nanoparticles differed significantly in an NaCl-concentration-dependent manner (Fig. 5A). Although the hydrodynamic diameter of the PEG-PAsp-coated magnetite nanoparticles did not change significantly up to 3 M NaCl, indicating the appreciable stability of the PEG-PAsp-coating, that of Resovist® significantly increased even at NaCl = 0.15 M, and reached more than 1 μm at NaCl = 0.5 M, due to the drastic aggregation. Note that the PEG-PAsp-coated nanoparticles did not show any change in

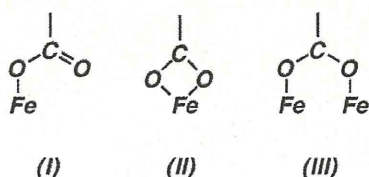


Fig. 4. Modes of carboxylate-metal complexation: monodentate (I), bidentate chelating (II), and bidentate bridging (III).

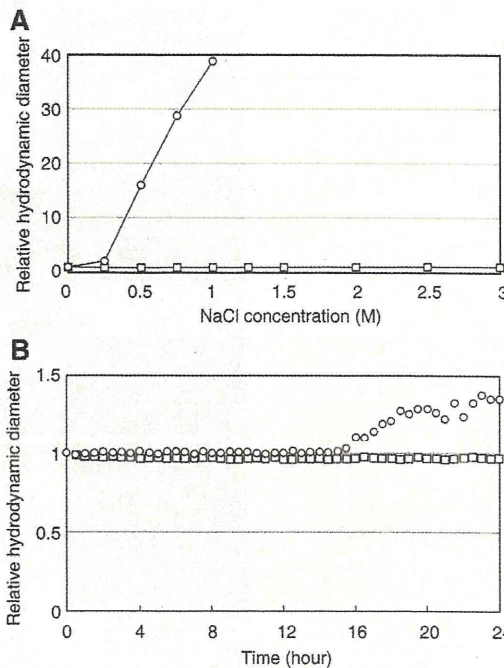


Fig. 5. NaCl concentration (A) and time (B) dependencies of the relative hydrodynamic diameter of magnetite nanoparticles, □: PEG-PAsp-coated nanoparticles, ○: dextran-coated nanoparticles (Resovist®). Fe concentration = 2 mmol/l; temperature = 37 °C; medium 10 mM Tris-HCl buffered saline (pH 7.4). 10% fetal bovine serum was contained in (B).

their size even after one month storage in 10 mM Tris-HCl buffered saline (pH 7.4, 37 °C) (data not shown).

The colloidal stability of the PEG-PAsp-coated magnetite nanoparticles in physiological conditions was also examined. We incubated them in 10 mM Tris-HCl buffered saline (pH 7.4) containing 10% fetal bovine serum at 37 °C for 24 h and measured the change of the hydrodynamic diameter (Fig. 5B). The size of the PEG-PAsp-coated magnetite nanoparticles did not obviously change during the 24-hour storage time. On the other hand, the size of Resovist® increased by the formation of aggregates after 16 h of storage time.

The stability of the PEG-PAsp-coated nanoparticles may come from the multivalent bonding between flanking carboxylic groups and the magnetite surface, as suggested by FT-IR study. These findings are consistent with a report showing that PEG-oligo(aspartic acid) block copolymer-coated iron oxide nanoparticles were stable at pH 2–11 and in 1 M NaCl, where the repeating number of aspartic acid units was 3 or more [20]. In contrast, instability of Resovist® against salt addition may be due to weak interaction between magnetite and hydroxyl groups of dextran [21].

3.4. MR imaging of experimental pancreatic cancer in vivo

The MR imaging of tumor tissue *in vivo* was then conducted by comparing PEG-PAsp- and dextran-coated magnetite nanoparticles, Resovist®. Resovist® has already been approved for clinical use as a liver-specific MRI contrast agent, due to accumulation into the reticuloendothelial system (RES) of the normal liver. Most malignant liver tumors do not contain RES cells and therefore are contrasted positive by Resovist®. A xenografted BxPC3 human pancreatic adenocarcinoma cell line in nude mice, characterized histologically by fibrosis and hypovascularity, was used as a model of intractable cancer. Recently, we reported that the administration of TGF- β inhibitor to tumor model mice significantly enhanced the intratumoral accumulation of nanoparticles encapsulating anticancer drugs [11]. Thus, we tested the effect of the *i.p.* administration of TGF- β

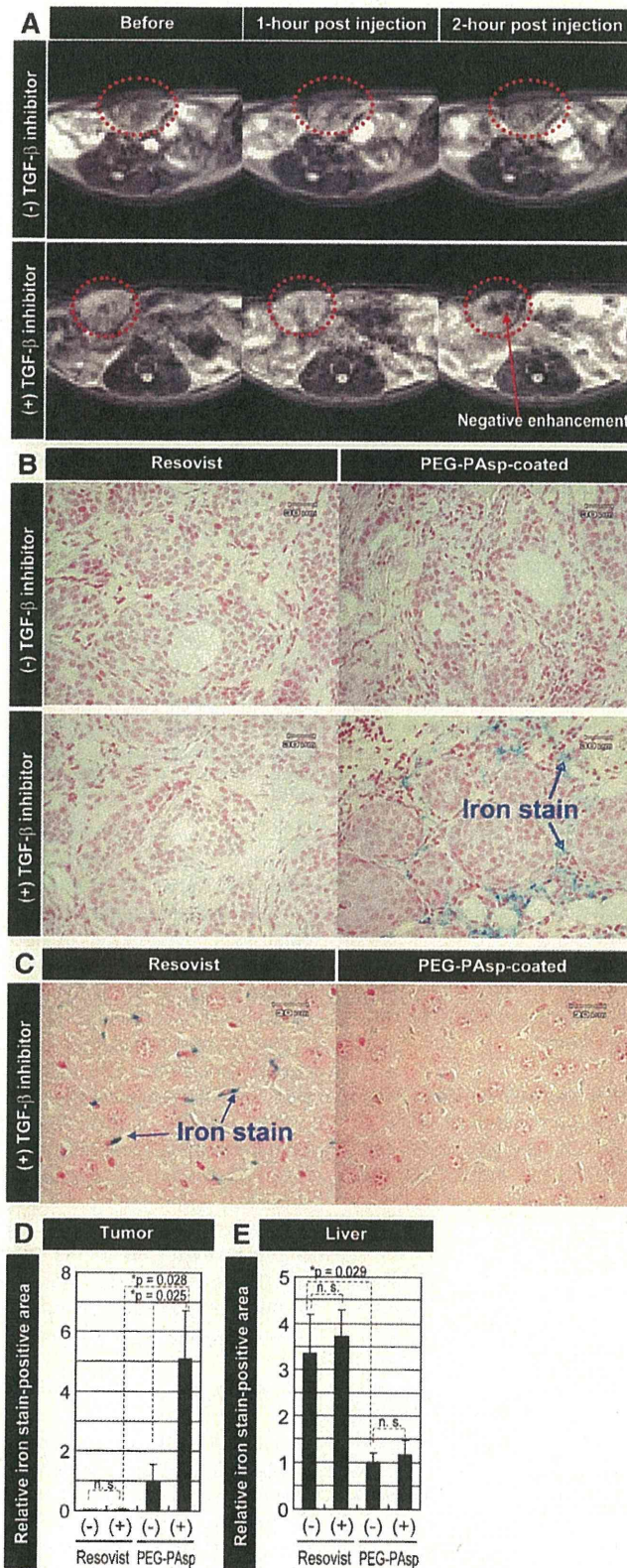


Fig. 6. MR imaging of experimental pancreatic cancer *in vivo* and the distribution of the nanoparticles in cancer and liver tissues. (A) T_2 -weighted images of tumor-implanted mice (tumor sites are circled by red dotted line) at different temporal points after injection of PEG-PAsp-coated magnetite nanoparticles and TGF- β inhibitor. All images were obtained in a field strength of 4.7 T. (B) Histological sections of BxPC3 xenograft stained with Prussian blue. The distribution of Resovist[®] and PEG-PAsp-coated magnetite nanoparticles, at 5.5 mg/kg with and without TGF- β inhibitor at 1 mg/kg, were examined 24 h after the administration. (C) Histological sections of liver stained with Prussian blue. The distribution of Resovist[®] and PEG-PAsp-coated magnetite nanoparticles, at 5.5 mg/kg with TGF- β inhibitor at 1 mg/kg, was examined 24 h after the administration. (D and E) Areas of iron staining in the tumor and liver were quantified. PEG-PAsp, PEG-PAsp coated magnetite nanoparticles with (+) and without (-) inhibitor. Error bars in the graphs represent standard errors of the mean ($n=6$), and P values were calculated by two-tailed Student's t test. n.s.: not significant.

inhibitor with the i.v. administration of Resovist® or the PEG–PAsp-coated magnetite nanoparticles on their imaging capability in size-matched xenografts of the BxPC3 cell line. Fig. 6A shows the T_2 -weighted MR images of the tumors at different time periods after the intravenous administration (preinjection, and 1 and 2 h postinjection) of PEG–PAsp-coated magnetite nanoparticles with and without TGF- β inhibitor.

Resovist® failed to image the tumor even with the co-administration of TGF- β inhibitor, presumably due to the non-specific accumulation into the reticuloendothelial system [8]. In contrast, the PEG–PAsp-coated magnetite nanoparticles exhibited significant negative enhancement of signal intensity in the tumor region of T_2 -weighted images when combined with TGF- β inhibitor, suggesting the accumulation of detectable amounts of the PEG–PAsp-coated magnetite nanoparticles within 2 h after injection. Therefore, the difference in behavior of these two types of magnetite nanoparticles *in vivo* had a crucial importance in achieving effective tumor accumulation for successful MR imaging.

To further verify the accumulation of iron oxide nanoparticles in the tumor, we performed Prussian blue staining of the tumor tissues to detect iron oxide, which stains blue. As shown in Fig. 6B, positive staining of the tumor for iron oxide was only obvious in the condition with PEG–PAsp-coated nanoparticles combined with the TGF- β inhibitor. Areas of iron staining in the tumor were then quantified as seen in Fig. 6D, demonstrating a significant increase in the areas of positive staining by TGF- β inhibitor treatment. The presence of iron oxide was consistent with the MRI results. Iron oxide was observed in the area rich in fibrotic components, suggesting that the administration of TGF- β inhibitor transiently increases the permeability of the tumor capillary to promote the extravasation of the PEG–PAsp-coated magnetite nanoparticles, even though the BxPC3 tumor has the characteristic of hypovascularity [11].

Lastly, we examined liver tissues from the mice treated with Resovist® or the PEG–PAsp-coated magnetite nanoparticle, with or without TGF- β inhibitor, by iron staining (Fig. 6C). Although aggregates of Resovist® accumulated in the liver, particularly in cells with smaller nuclei (presumably Kupffer cells), far less PEG–PAsp-coated magnetite nanoparticles accumulated in the liver without aggregation. These results did not differ with or without TGF- β inhibitor, which was determined by the area of Prussian blue staining (Fig. 6E).

4. Conclusion

In conclusion, we here demonstrated the physicochemical properties of PEG–PAsp-coated magnetite nanoparticles and the feasibility of these nanoparticles as MR contrast agents for cancer diagnosis. Improving the stability of nanoparticles might be important for enabling a longer half-life in the bloodstream and a better accumulation in tumor tissue, leading to effective MR imaging with contrast agents. The neutral ζ -potential of the PEG–PAsp-coated nanoparticle may contribute to avoidance of reticuloendothelial system uptake. Formation of the stable and dense PEG layer on the magnetite surface through the anchoring of PEG–PAsp by the monodentate chelation of COO⁻ residues to iron atoms definitely plays a substantial role in the increased stability of the nanoparticles *in vivo*. The use of PEG–PAsp-coated magnetite nanoparticles combined with a TGF- β inhibitor could thus become a novel regime in the diagnosis of intractable cancers, including pancreatic adenocarcinoma.

Acknowledgements

The authors thank Dr James R. Christie II, The University of Tokyo, for editing the English of the manuscript. This work was supported by a Grant-in-Aid for Scientific Research from the Ministry of Education, Culture, Sports, Science and Technology (MEXT), Core Research for

Evolution of Science and Technology (CREST), Japan Science and Technology Corporation (JST), and the 21st century COE program 'Human-Friendly Materials based on Chemistry' from MEXT.

Appendix A. Supplementary data

Supplementary data associated with this article can be found, in the online version, at doi:10.1016/j.jconrel.2009.06.002.

References

- [1] M.R. Dreher, W. Liu, C.R. Michelich, M.W. Dewhirst, F. Yuan, A. Chilkoti, Tumor vascular permeability, accumulation, and penetration of macromolecular drug carriers, *J. Natl. Cancer Inst.* 98 (5) (2006) 335–344.
- [2] H.A. Burris, M.J. Moore, J. Andersen, M.R. Green, M.L. Rothenberg, M.R. Modiano, M.C. Cripps, R.K. Portenoy, A.M. Storniolo, P. Tarassoff, R. Nelson, F.A. Dorr, C.D. Stephens, D.D. Von Hoff, Improvements in survival and clinical benefit with gemcitabine as first-line therapy for patients with advanced pancreas cancer: a randomized trial, *J. Clin. Oncol.* 15 (6) (1997) 2403–2413.
- [3] D.V. Sahani, Z.K. Shah, O.A. Catalano, G.W. Boland, W.R. Brugge, Radiology of pancreatic adenocarcinoma: current status of imaging, *J. Gastroenterol. Hepatol.* 23 (1) (2008) 23–33.
- [4] D.L. Huber, Synthesis, properties, and applications of iron nanoparticles, *Small* 1 (5) (2005) 482–501.
- [5] R. Weissleder, G. Elidonzo, J. Wittenberg, C.A. Rabito, H.H. Bengel, L. Josephson, Ultrasmall superparamagnetic iron oxide: characterization of a new class of contrast agents for MR imaging, *Radiology* 175 (2) (1990) 489–493.
- [6] M. Lewin, N. Carlesso, C.H. Tung, X.W. Tang, D. Cory, D.T. Scadden, R. Weissleder, Tat peptide-derivatized magnetic nanoparticles allow *in vivo* tracking and recovery of progenitor cells, *Nat. Biotechnol.* 18 (4) (2000) 410–414.
- [7] Y.W. Jun, J.H. Lee, J. Cheon, Chemical design of nanoparticle probes for high-performance magnetic resonance imaging, *Angew. Chem. Int. Ed.* 47 (28) (2008) 5122–5135.
- [8] D.D. Stark, R. Weissleder, G. Elizondo, et al., Superparamagnetic iron oxide: clinical application as a contrast agent for MR imaging of the liver, *Radiology* 168 (2) (1988) 297–301.
- [9] T. Neuberger, B. Schöpf, H. Hofmann, M. Hofmann, B. von Rechenberg, Superparamagnetic nanoparticles for biomedical applications: possibilities and limitations of a new drug delivery system, *J. Magn. Mater.* 293 (1) (2005) 483–496.
- [10] M. Kumagai, Y. Imai, T. Nakamura, Y. Yamasaki, M. Sekino, S. Ueno, K. Hanaoka, K. Kikuchi, T. Nagano, E. Kaneko, K. Shimokado, K. Kataoka, Iron hydroxide nanoparticles coated with poly(ethylene glycol)-poly(aspartic acid) block copolymer as novel magnetic resonance contrast agents for *in vivo* cancer imaging, *Colloids Surf. B: Biointerfaces* 56 (1–2) (2007) 174–181.
- [11] M.R. Kano, Y. Bae, C. Iwata, Y. Morishita, M. Yashiro, M. Oka, T. Fujii, A. Komuro, K. Kiyono, M. Kaminishi, K. Hirakawa, Y. Ouchi, N. Nishiyama, K. Kataoka, K. Miyazono, Improvement of cancer-targeting therapy, using nanocarriers for intractable solid tumors by inhibition of TGF- β signaling, *Proc. Natl. Acad. Sci. U. S. A.* 104 (9) (2007) 3460–3465.
- [12] Y. Matsumura, H. Maeda, A new concept for macromolecular therapeutics in cancer-chemotherapy-mechanism of tumorotropic accumulation of proteins and the antitumor agent SMANCS, *Cancer Res.* 46 (12) (1986) 6387–6392.
- [13] N. Nishiyama, M. Yokoyama, T. Aoyagi, T. Okano, Y. Sakurai, K. Kataoka, Preparation and characterization of self-assembled polymer-metal complex micelle from cis-dichlorodiammineplatinum(II) and poly(ethylene glycol)-poly(alpha,beta-aspartic acid) block copolymer in an aqueous medium, *Langmuir* 15 (2) (1999) 377–383.
- [14] E. Fukushima, S.B.W. Roeder (Eds.), *Experimental pulse NMR: a nuts and bolts approach*, Addison-Wesley, Reading, Mass, 1981, pp. 28–35.
- [15] A.J.S. MacFadzean, L.J. Davis, Iron-staining erythrocytic inclusions with especial reference to acquired haemolytic anaemia, *Glasgow Med. J.* 28 (1947) 237–279.
- [16] S. Takae, Y. Akiyama, H. Otsuka, T. Nakamura, Y. Nagasaki, K. Kataoka, Ligand density effect on biorecognition by PEGylated gold nanoparticles: regulated interaction of RCA120 lectin with lactose installed to the distal end of tethered PEG strands on gold surface, *Biomacromolecules* 6 (2) (2005) 818–824.
- [17] L. Cromières, V. Moulin, B. Fourest, E. Giffaut, Physico-chemical characterization of the colloidal hematite/water interface: experimentation and modeling, *Colloids Surf., A. Physicochem. Eng. Asp.* 202 (1) (2002) 101–115.
- [18] L.J. Kirwan, P.D. Fawell, W. van Bronswijk, In situ FTIR-ATR examination of poly(acrylic acid) adsorbed onto hematite at low pH, *Langmuir* 19 (14) (2003) 5802–5807.
- [19] Y.X.J. Wang, S.M. Hussain, G.P. Krestin, Superparamagnetic iron oxide contrast agents: physicochemical characteristics and applications in MR imaging, *Eur. Radiol.* 11 (11) (2001) 2319–2331.
- [20] S.R. Wan, J.S. Huang, M. Guo, H. Zhang, Y. Cao, H. Yan, K. Liuet, Biocompatible superparamagnetic iron oxide nanoparticle dispersions stabilized with poly(ethylene glycol)oligo(aspartic acid) hybrids, *J. Biomed. Mater. Res. A* 80A (4) (2007) 946–954.
- [21] C.W. Jung, Surface-properties of superparamagnetic iron-oxide MR contrast agents – ferumoxides, ferumoxtran, ferumoxsil, *Magn. Reson. Imaging* 13 (5) (1995) 675–691.



Design and development of dendrimer photosensitizer-incorporated polymeric micelles for enhanced photodynamic therapy[☆]

Nobuhiro Nishiyama^{a,c}, Yuji Morimoto^d, Woo-Dong Jang^e, Kazunori Kataoka^{a,b,c,*}

^a Center for Disease Biology and Integrative Medicine, Graduate School of Medicine, the University of Tokyo, Tokyo, Japan

^b Department of Materials Engineering, Graduate School of Engineering, the University of Tokyo, Tokyo, Japan

^c Center for Nano-Bio Integration, the University of Tokyo, Tokyo, Japan

^d Department of Integrative Physiology and Bio-Nano Medicine, National Defense Medical College, Saitama, Japan

^e Department of Chemistry, College of Science, Yonsei University, Seoul, Republic of Korea

ARTICLE INFO

Article history:

Received 13 November 2008

Accepted 26 January 2009

Available online 4 February 2009

Keywords:

Photodynamic therapy (PDT)

Photosensitizers (PSs)

Dendrimers

Polymeric micelles

Photodynamic diagnosis (PDD)

Photochemical internalization (PCI)

ABSTRACT

Photodynamic therapy (PDT), which involves systemic administration of photosensitizers (PSs) followed by local photoillumination, is a promising method for the treatment of solid tumors and other diseases. Recently, considerable efforts have been devoted to the development of nanocarriers for the PS delivery with the aim of avoiding non-specific phototoxicity to normal tissues such as the skin. Here, we discuss the biological significance of the use of nanocarrier-encapsulated PSs in PDT. Also, we report our recent achievements on the development of dendrimer photosensitizer-loaded micelles as nanocarriers for PS delivery. We found that our nanocarriers greatly enhanced the PDT efficacy *in vitro* and *in vivo*, and also significantly reduced the skin phototoxicity. These results indicate the importance of a development strategy for nanocarriers and their great potential for clinical use. In addition, this review discusses the development of nanocarriers for emerging PDT-related technologies such as photodynamic diagnosis (PDD) and photochemical internalization (PCI).

© 2009 Elsevier B.V. All rights reserved.

Contents

1. Introduction	327
2. Photodynamic therapy (PDT) with nanocarrier-encapsulated photosensitizers (PSs)	328
2.1. Biodistribution of nanocarrier-encapsulated PSs	328
2.2. <i>In vivo</i> mechanisms of PDT	329
3. Polymeric micelles encapsulating dendrimer photosensitizers for enhanced PDT	330
3.1. Development of dendrimer photosensitizer-loaded micelles	330
3.2. <i>In vitro</i> PDT effect of dendrimer photosensitizer-loaded micelles	331
3.3. <i>In vivo</i> PDT effect of dendrimer photosensitizer-loaded micelles	333
4. Photodynamic diagnosis (PDD)-guided PDT	333
5. Development of light-sensitive nanocarriers utilizing photochemical internalization (PCI)	334
6. Conclusion	336
Acknowledgments	336
References	336

1. Introduction

Photodynamic therapy (PDT) is a promising method for the localized treatment of several diseases, including solid tumors [1–3]. PDT involves the systemic administration of photosensitizers (PSs) such as porphyrin and phthalocyanine derivatives, followed by photoactivation of PSs at the disease site with light of a specific wavelength. As illustrated in Fig. 1, PSs in a singlet state at the lowest or ground

[☆] This review is part of the *Advanced Drug Delivery Reviews* theme issue on "Controlling Oxidative Stress: Therapeutic and Delivery Strategies".

* Corresponding author. Department of Materials Engineering, Graduate School of Engineering, The University of Tokyo, 7-3-1 Hongo, Bunkyo-ku, Tokyo 113-8656, Japan. Tel.: +81 3 5841 7138; fax: +81 3 5841 7139.

E-mail address: kataoka@bmiw.t.u-tokyo.ac.jp (K. Kataoka).